Università degli Studi di Napoli “Federico II”

SCUOLA POLITECNICA E DELLE SCIENZE DI BASE
DIPARTIMENTO DI INGEGNERIA INDUSTRIALE

CORSO DI LAUREA IN INGEGNERIA AEROSPAZIALE

CLASSE DELLE LAUREE IN INGEGNERIA INDUSTRIALE (L-9)

Elaborato di laurea in Meccanica del Volo

Geometric modelling, stability and control analysis of the unmanned aerial vehicle General Atomics RQ-1 Predator with OpenVSP

Relatore:
Prof. Danilo Ciliberti

Candidato:
Sessa Francesco
Matr. N35004218

ANNO ACCADEMICO 2023 – 2024

Alla mia migliore amica Simona,
A mio fratello Andrea, il mio miglior professore di matematica e fisica,
Alla mia famiglia.

Abstract

The purpose of this work is the geometric modelling and preliminary aerodynamic analysis of the General Atomics RQ-1 Predator UAV. To carry out this project, the open-source OpenVSP software was used. It allows the user to model the shape of the aircraft and perform an aerodynamic analysis using the VSPAERO tool. This tool works with the vortex lattice method (VLM), a numerical method based on Biot-Savart's law. The results obtained were then organized using Microsoft Excel to perform the longitudinal and latero-directional stability and control analysis of the aircraft. The main aerodynamic coefficients, as well as wing and tailplane aerodynamic loadings for different sets, were analyzed to show the effect of individual components. The analyses were done in different configurations also to highlight the effect of control surfaces. From the slopes of the obtained curves, it was then possible to derive the static stability and control derivatives of the aircraft.

Sommario

Lo scopo di questo lavoro è la modellazione geometrica e l'analisi aerodinamica preliminare dell'UAV General Atomics RQ-1 Predator. Per realizzare questo progetto è stato utilizzato il software open-source OPENVSP che permette all'utente di modellare la forma del velivolo ed effettuare un'analisi aerodinamica adoperando il tool VSPAERO. Questo tool utilizza il vortex lattice method (VLM), un metodo numerico basato sulla legge di Biot-Savart. I risultati ottenuti sono stati poi organizzati utilizzando Microsoft Excel per effettuare l'analisi di stabilità e controllo longitudinale e latero-direzionale del velivolo. Sono stati analizzati i principali coefficienti aerodinamici e i carichi aerodinamici dell'ala e del piano di coda per diversi set, per mostrare l'effetto dei singoli componenti. Le analisi sono state effettuate in diverse configurazioni per evidenziare anche l'effetto delle superfici mobili. Dalle pendenze delle curve ottenute, è stato poi possibile ricavare le derivate di stabilità statica e di controllo del velivolo.

Table of contents

List of figures

List of tables

1. Introduction

1.1 Objectives

The objective of this thesis is to evaluate the longitudinal and latero-directional control and stability of the General Atomics RQ-1 Predator UAV using the software OpenVSP. The latter allows a preliminary aerodynamic analysis to be carried out using the VSPAERO tool. By collecting the results obtained, it is possible to assess the stability and control derivatives, and the performance of its control surfaces, in particular the performance of the inverted V-shaped tailplane.

1.2 Layout of the work

Chapter 1: This chapter presents the thesis and the aircraft RQ-1 predator.

Chapter 2: This chapter describes the theory behind the vortex lattice method, the numerical method applied to compute the analysis.

Chapter 3: This chapter shows how the RQ-1 predator model has been created in OpenVSP.

Chapter 4: In this chapter is discussed the longitudinal aerodynamics analysis based on the results obtained.

Chapter 5: In this chapter is discussed the lateral and directional aerodynamics analysis based on the results obtained.

1.3 General Atomics RQ-1 Predator

The RQ-1 Predator (Figure 1.1) is an American unmanned aerial vehicle (UAV) built by General Atomics. In particular, the RQ-1 is designed for military missions such as aerial surveillance and reconnaissance, indeed the Predator carries cameras and other sensors. The RQ-1 Predator features an inverted V-tail that operates as an all-moving control surface, specifically acting as ruddervators, which function as rudders when moving differentially and as elevators when moving together [1]. The vertical tail, on the other hand, acts only as a lateral-directional stabilizer. Such empennage configuration is also useful to avoid the propeller strike at take-off rotation. The aircraft is powered by a Rotax engine and driven by a two-bladed propeller in a pusher configuration.

Figure 1.1 – General Atomics RQ-1 Predator

1.4 OpenVSP

OpenVSP is a parametric aircraft geometry tool developed by NASA. OpenVSP allows the user to create a 3D model of an aircraft defined by common engineering parameters. This model can be processed into formats suitable for engineering analysis as aerodynamic or structural analysis. It provides a large number of basic geometries (Figure 1.2), which users can modify and assemble to create models [2].

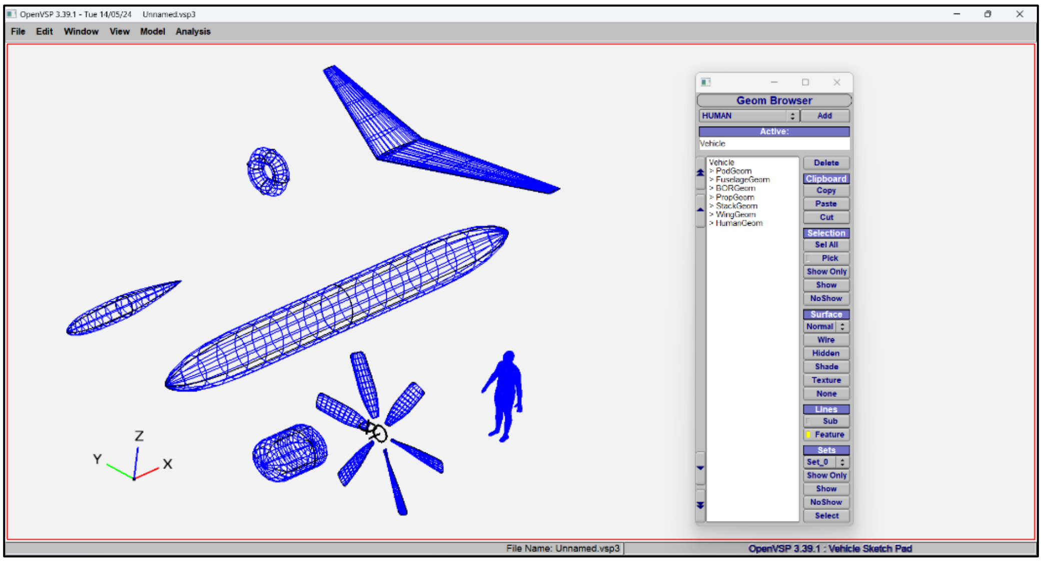

Figure 1.2 – OpenVSP graphical interface and a few base geometry models provided

2. Vortex Lattice Method

VSPAERO allows the user to choose between two options Vortex Lattice Method (VLM) and Panel method. The first will be treated more in detail in this chapter as it is the one applied in this project.

2.1 Theorical background

2.1.1 Flow assumptions

The VLM the method is based on the following assumptions:

- The flow field is incompressible, inviscid and irrotational;
- Lifting surfaces are thin and the influence of thickness on aerodynamic forces is neglected;
- Small angle of attack and sideslip;

Due to incompressibility and irrotationality of the flow is possible to state that the gradient of the velocity vector V and its rotor, called also vorticity ξ, are zero:

$$\nabla \cdot V = 0 \tag{2.1}$$

$$\xi = \nabla \times V = 0 \tag{2.2}$$

By (2.2) we can say that the velocity field is a potential field, which means that the kinetic potential function Φ exists so that:

$$V = \nabla \Phi \tag{2.3}$$

Φ is also known as velocity potential. Due to (2.1) with a substitution is possible to state that:

$$\nabla V = \nabla^2 \Phi = 0 \tag{2.4}$$

This means that Φ is an harmonic function since it is the solution of a Laplace equation. Harmonic functions possess the property of linearity, meaning that a linear combination of harmonic functions is still an harmonic function and a solution of Laplace's equation. This means that we can see the velocity potential of a complicated velocity field as the sum of potentials of simpler velocity fields that are still incompressible, inviscid and irrotational.

2.1.2 *Degenerated Geometry*

As previously stated, the VLM does not consider the thickness of the model, instead it considers a degenerated geometry built from the model. The lifting components are replaced with their mean surface while the fuselage is simplified into two mean surfaces arranged to make a cross-shaped body (Figure 2.1).

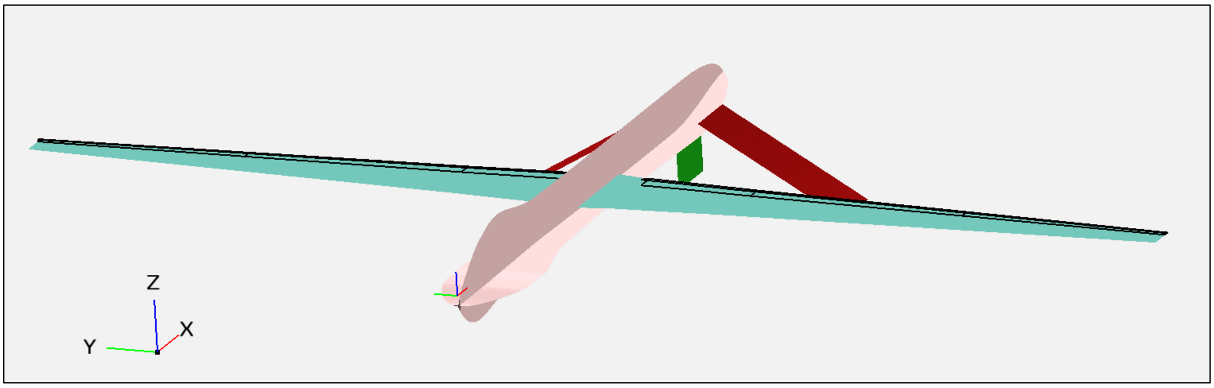

Figure 2.1 – Degenerated geometry of RQ-1's model

2.1.3 *Boundary conditions*

To find Φ a boundary conditions is needed. The boundary condition applied by the VLM is the impermeability of the surfaces, meaning that the normal component of the velocity on the surfaces is zero, so the velocity must be tangent to the surfaces. This implies:

$$V \cdot n = \nabla\Phi \cdot n = 0 \tag{2.5}$$

Where n is the vector orthogonal to the surface point by point. Under the thin surfaces assumption, this condition can be linearized on the mean surfaces, thus instead of applying the (2.5) on the original surface, the VLM simplifies the problem imposing the boundary condition on the degenerated geometry.

2.1.4 *Vortex Ring*

The VLM usually models the wing into a finite number of panels (chordwise and spanwise), which the solver models up as triangles, quadrilaterals and polygons. These polygons are considered as vortex rings, meaning portions of surfaces with a certain circulation Γ (Figure 2.2).

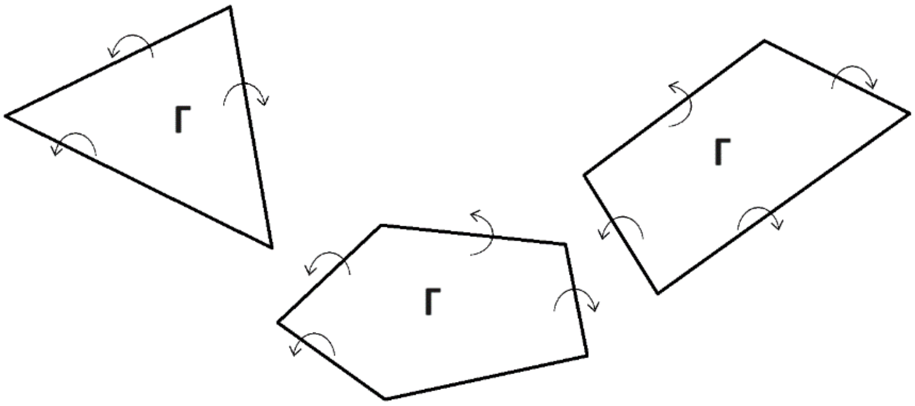

Figure 2.2 – Ring vortices

Each vortex ring generates an induced velocity. In order to evaluate the total aerodynamic force, the contribution of all rings must be summed. Given a point *P* and a group of vortex rings *G*, if *P* is far away from *G*, the solver can simplify *G* into a single vortex ring to speed up the calculations and to decrease the computational effort [4].

2.1.5 Biot-Savart's law

Known the vortex strength, the induced velocity in a point P can be computed with the Biot-Savart's law:

$$V_P = \frac{\Gamma}{4\pi} \int \frac{dl \cdot r_P}{|r_P|^3} \tag{2.6}$$

Where Γ is the vortex circulation called also vortex strength.

2.2 Solution process

As said, the function Φ can be considered the sum of simpler kinetic potentials. Similar considerations apply to the velocity because of the linearity of the derivate operator. For the VLM the velocity is divided into these terms:

- V_∞ is the velocity of the flow infinitely far from the body;
- V_i is the induced velocity by the vortices given by the sum of the velocity induced by the loops (the finite vortex filament) and by the wakes (the two infinite vortices filaments):

$$V_i = \sum_j^{Loops} \left[V_{loop}\right]_j + \sum_j^{Wakes} \left[V_{wake}\right]_j \tag{2.7}$$

- V_{rotors} is any rotor downwash models;

Then, by applying the boundary conditions (2.5) and (2.6):

$$(V_\infty + V_{\text{rotors}} + V_{\text{i}}) \cdot n = 0 \tag{2.8}$$

This results in a linear system for the unknow circulations strengths Γ_{i}:

$$A\overrightarrow{\Gamma_\iota} = \vec{b} \tag{2.9}$$

This linear system is than solved with a preconditioned GMRES, an iterative method for numerical solutions [4].

3. Geometric Modelling

3.1 General aspects of the model

3.1.1 *Model's components*

The model (Figure 3.2) has been realized referring to the following drawings (Figure 3.1) exploiting the tool 3D background of OpenVSP.

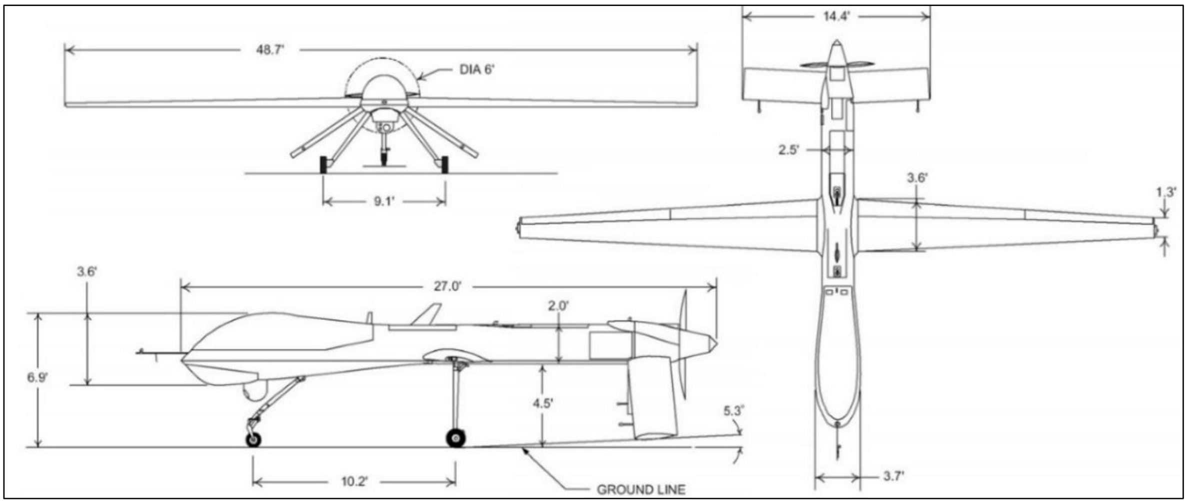

Figure 3.1 – RQ-1 drawings [5]

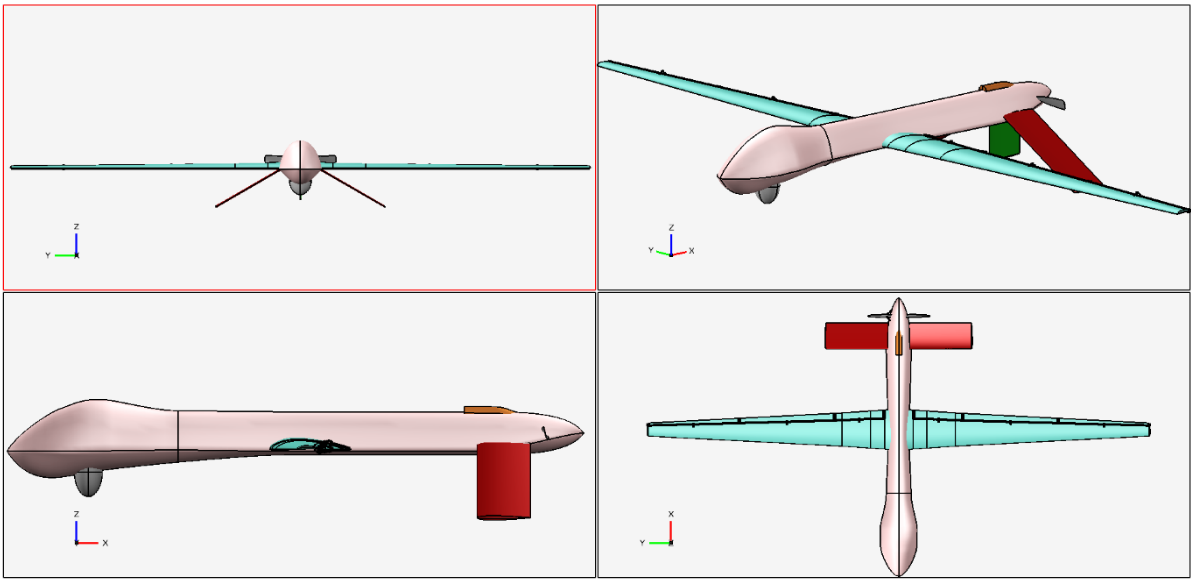

Figure 3.2 – RQ-1 model's four views

The model built consists of the components below:

- All_Comp: a blank parent of all the other components to move them together easily;
- Fuselage;
- Wing;
- Center_of_gravity: a blank to remember the position of the gravity centre chosen;
- VerticalTailplane;
- Right/left ruddervators: they are two different components to rotate them asymmetrically;
- Right/left_ruddervators_Ref: two blanks placed at the 25% of the root chord of both ruddervators;
- Ruddervator_Group: a blank to move together the ruddervators;
- Propeller/Inlet/Camera: other components modelled but not considered in the analysis.

3.1.2 Mesh

OpenVSP automatically generates a mesh on the model built (Figure 3.3) whose parameters can be chosen by the user. Specifically, the user can refine the number of slices for each component by modifying Num_W (chordwise) and Num_U (spanwise) parameters or changing the component's clustering.

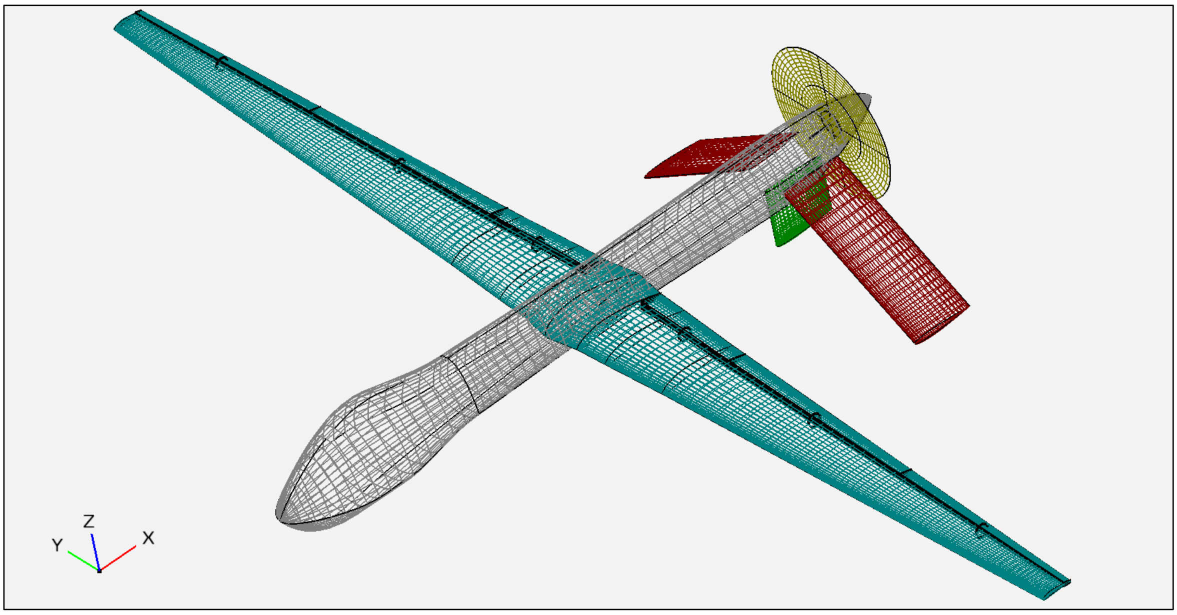

Figure 3.3 – Mesh of RQ-1 model

3.2 Component specifications

3.2.1 Fuselage

The fuselage (Figure 3.4) has been divided into 6 sections the first and last are the edges, the others are a super-ellipse type section. It is 27 feet long and its refinement is Num_W=41, Num_U=67.

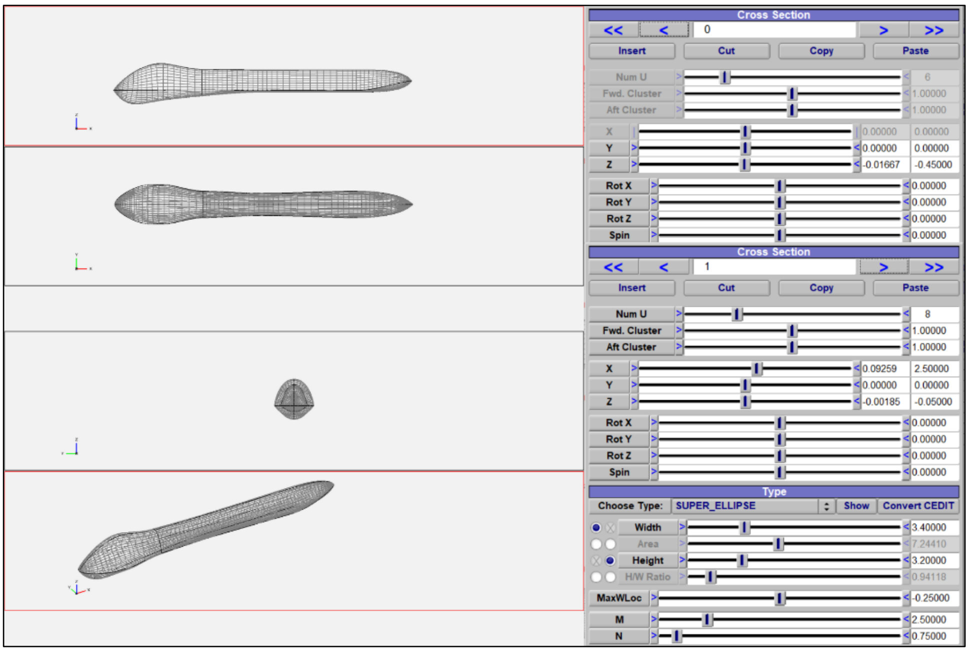

0

Num U 6
Fwd. Cluster 1.00000
Aft Cluster 1.00000
X 0.00000 0.00000
Y 0.00000 0.00000
Z -0.01667 -0.45000
Rot X 0.00000
Rot Y 0.00000
Rot Z 0.00000
Spin 0.00000

1

Num U 8
Fwd. Cluster 1.00000
Aft Cluster 1.00000
X 0.09259 2.50000
Y 0.00000 0.00000
Z -0.00185 -0.05000
Rot X 0.00000
Rot Y 0.00000
Rot Z 0.00000
Spin 0.00000

Choose Type: SUPER_ELLIPSE
● Width 3.40000
○ ○ Area 7.24410
● Height 3.20000
○ ○ H/W Ratio 0.94118
MaxWLoc -0.25000
M 2.50000
N 0.75000

Figure 3.4 – Parameters of fuselage's cross sections 0 and 1

3.2.2 Wing

The airfoil chosen is a NACA 6412 (Figure 3.5), except for section 0 (root profile) where a NACA 6423 was chosen to simulate the wing connection to the fuselage.

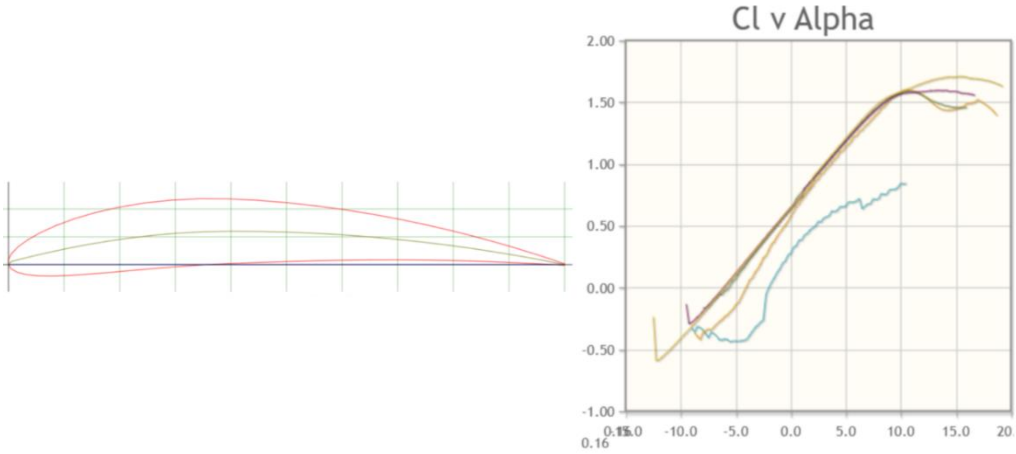

Figure 3.5 – NACA 6412 airfoil and his Cl v Alpha [6]

The wing has been composed of 4 sections, with a span of 48.58 ft and an aspect ratio of 19.14. The refinement is Num_W=61, Num_U=71 and a tip clustering of 0.25 for section 4. The control surfaces cover the entire wing along the wingspan and are divided into: Inner Flaps, Outer Flaps and Ailerons (Figure 3.6). They have been modelled using the Sub tool of OpenVSP.

Span 48.58000
Proj Span 48.58000
Chord 3.31557
Area 123.30061
Aspect Ratio 19.14035

Coord System: Rel
XLoc 12.100 12.100
YLoc 0.000 0.000
ZLoc -0.340 -0.340
XRot 0.000 0.000
YRot 0.000 0.000
ZRot 0.000 0.000
Rot Origin(X) 0.000
About: 1 Wing, Attach
Planar: XZ
Axial: None
N 2

NAME	TYPE	SURF
InnerFlaps	Control_Surf	Surf_0
Ailerons	Control_Surf	Surf_0
OuterFlaps	Control_Surf	Surf_0

Type Control_Surf
Surface Surf_0
Name Ailerons
Tag Inside
Upper/Lower Both
Start U 0.706000
End U 0.800000
Start Eta 0.636422
End Eta 1.000000
Length/C, Constant
Start Length 0.541625
Start Length/C 0.250000
End Length 0.312500
End Length/C 0.250000

Figure 3.6 – Some parameters of the wing and ailerons

3.2.3 Tailplane

The vertical tailplane acts only as a stabiliser. It is a straight, untapered vertical wing with a 2.4 ft span and 2.5 ft chord. The ruddervator (Figure 3.7) has been modelled as two different wings whose parameters are linked with the AdvLink tool and attached to the blank Ruddervator_Group to position them symmetrically. Since it is an all-moving control surface, it has been modelled as two components to easily deflect them symmetrically and differently with the UserParms created. The total projected span of the ruddervator projected in the horizontal plane is 14 ft, with a negative dihedral angle of 30 degrees. The refinement is Num_W=41, Num_U=21 with a tip cluster of 0.5. For both the vertical and ruddervator a NACA 0008 profile has been chosen. The left ruddervator is simply a right-wing shifted to the left. To correctly position it, during the modelling the link RuddervatorRightLeftLink (Figure 3.8) has been created and then both have been attached to the blank RuddervatoGroup.

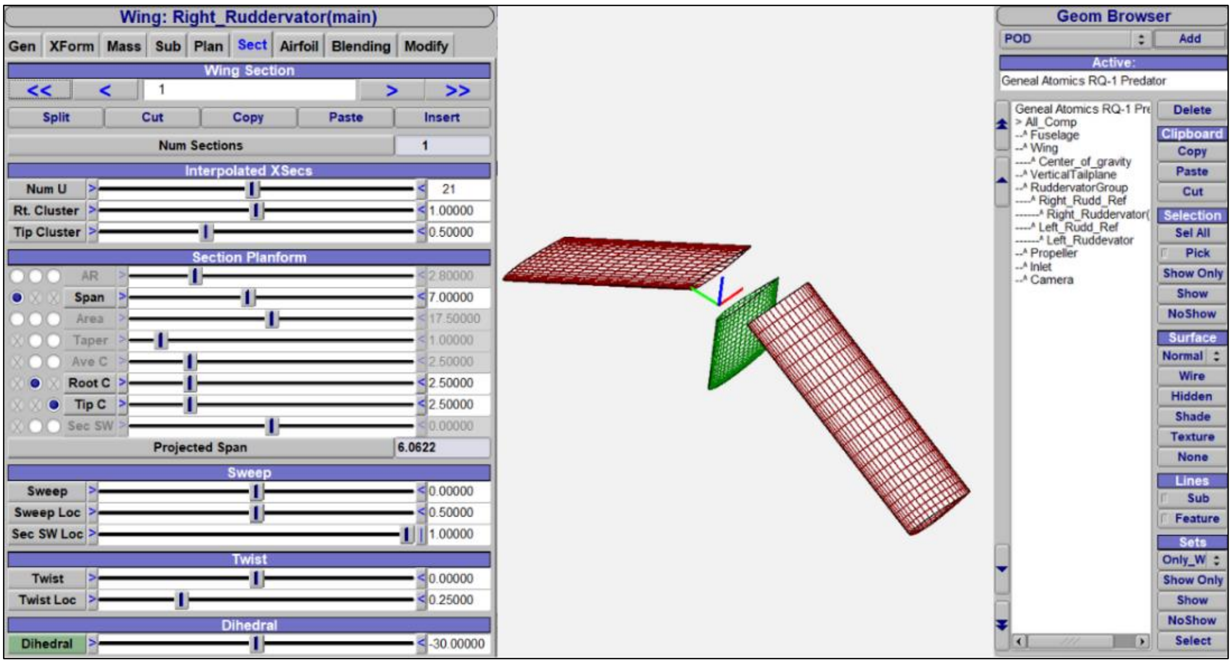

Wing Section: 1
Num Sections: 1
Num U: 21
Rt. Cluster: 1.00000
Tip Cluster: 0.50000
AR: 2.80000
Span: 7.00000
Area: 17.50000
Taper: 1.00000
Ave C: 2.50000
Root C: 2.50000
Tip C: 2.50000
Sec SW: 0.00000
Projected Span: 6.0622
Sweep: 0.00000
Sweep Loc: 0.50000
Sec SW Loc: 1.00000
Twist: 0.00000
Twist Loc: 0.25000
Dihedral: -30.00000

Figure 3.7 – Some tailplane parameters

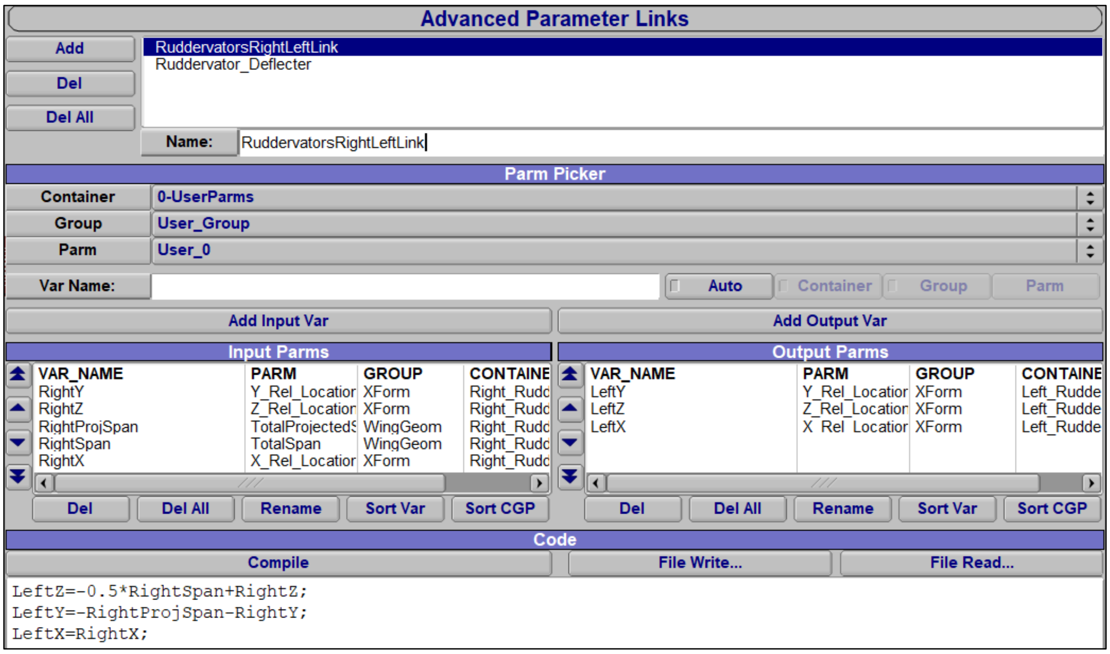

RuddervatorsRightLeftLink
Ruddervator_Deflecter

Name: RuddervatorsRightLeftLink
Container: 0-UserParms
Group: User_Group
Parm: User_0
Var Name:

Input Parms

VAR_NAME	PARM	GROUP	CONTAINE
RightY	Y_Rel_Locatior	XForm	Right_Rudc
RightZ	Z_Rel_Locatior	XForm	Right_Rudc
RightProjSpan	TotalProjected!	WingGeom	Right_Rudc
RightSpan	TotalSpan	WingGeom	Right_Rudc
RightX	X_Rel_Locatior	XForm	Right_Rudc

Output Parms

VAR_NAME	PARM	GROUP	CONTAINE
LeftY	Y_Rel_Locatior	XForm	Left_Rudde
LeftZ	Z_Rel_Locatior	XForm	Left_Rudde
LeftX	X_Rel_Locatior	XForm	Left_Rudde

```
LeftZ=-0.5*RightSpan+RightZ;
LeftY=-RightProjSpan-RightY;
LeftX=RightX;
```

Figure 3.8 – The Advanced Link RuddervatorRightLeftLink

Then, to easily deflect them symmetrically and asymmetrically two user parms have been created, linked to the rotation of the blank components positioned at the 25% of the root chord of both the ruddervators, to which the latter were attached. To obtain a realistic rotation about the local span direction (a reference system rotated about the longitudinal axis by the tail dihedral angle), the custom UserParm simultaneously rotates the ruddervators about the global Y and Z axes by the cosine and sine of the tail dihedral angle, respectively (Figure 3.9).

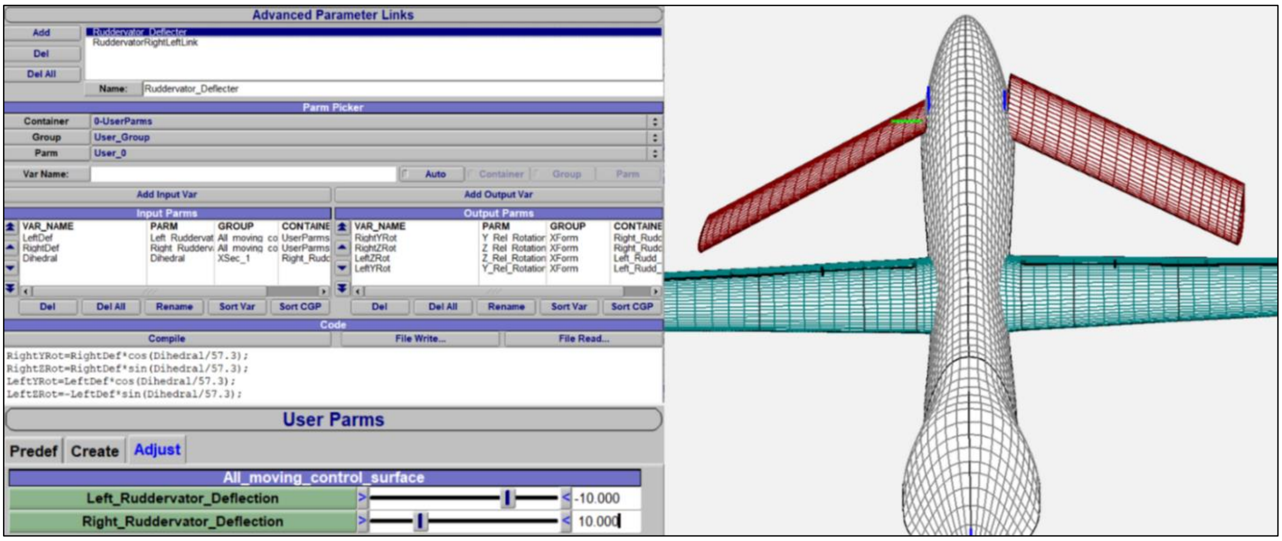

Ruddervator_Deflecter
RuddervatorRightLeftLink

Name: Ruddervator_Deflecter

Container: 0-UserParms
Group: User_Group
Parm: User_0
Var Name:

VAR_NAME	PARM	GROUP	CONTAINE
LeftDef	Left_Ruddervat	All_moving_co	UserParms
RightDef	Right_Rudderv	All_moving_co	UserParms
Dihedral	Dihedral	XSec_1	Right_Rudc

VAR_NAME	PARM	GROUP	CONTAINE
RightYRot	Y_Rel_Rotation	XForm	Right_Rudc
RightZRot	Z_Rel_Rotation	XForm	Right_Rudc
LeftZRot	Z_Rel_Rotation	XForm	Left_Rudd_
LeftYRot	Y_Rel_Rotation	XForm	Left_Rudd_

```
RightYRot=RightDef*cos(Dihedral/57.3);
RightZRot=RightDef*sin(Dihedral/57.3);
LeftYRot=LeftDef*cos(Dihedral/57.3);
LeftZRot=-LeftDef*sin(Dihedral/57.3);
```

All_moving_control_surface
Left_Ruddervator_Deflection -10.000
Right_Ruddervator_Deflection 10.000

Figure 3.9 – The User Parms created and the ruddervator deflected asymmetrically

4. Longitudinal Aerodynamic Analysis

4.1 VSPAERO parameters

4.1.1 Geometry Sets

There are various parameters that the user can choose before running the VLM analysis on VSPAERO, first of all the geometry set must be chosen. To evaluate the effects of each component, the same analysis was carried out on the following sets:

•W: containing only the wing;
•WR: containing the wing and the ruddervators, hence only the lifting surfaces;
•WF: containing the wing and the fuselage;
•WFT: containing the wing, the fuselage and the tailplane, that is the complete aircraft.
For all sets the reference area and lengths chosen are from the wing. The propeller, the camera and the engine’s nacelle are neglected in the analysis.

4.1.2 Flow conditions

According to the RQ-1 cruise speed, the input parameters chosen are:

- A Mach number equal to 0.1;
- A Reynolds number of 10 million;
- A set of values of the angle of attack alpha from 0 to 12 degrees, with a step of 2 degrees, hence 7 points overall.

4.1.3 Center of gravity

In this project the mass properties have not been characterized for each component, instead the center of gravity has been inserted manually. It has been positioned at the 30% of the mean chord computed by OpenVSP, shown in Figure 3.6, hence its position has been calculated as follows:

$$X_G = 0.30 \cdot \mathrm{MeanChord} + \mathrm{XlocWing} = 0.30 \cdot 3.31557 \text{ ft} + 12.1 \text{ ft} = 13.094 \text{ ft} \quad (4.1)$$

while its Y and Z coordinates chosen are null, by the symmetry of the aircraft (Figure 4.1).

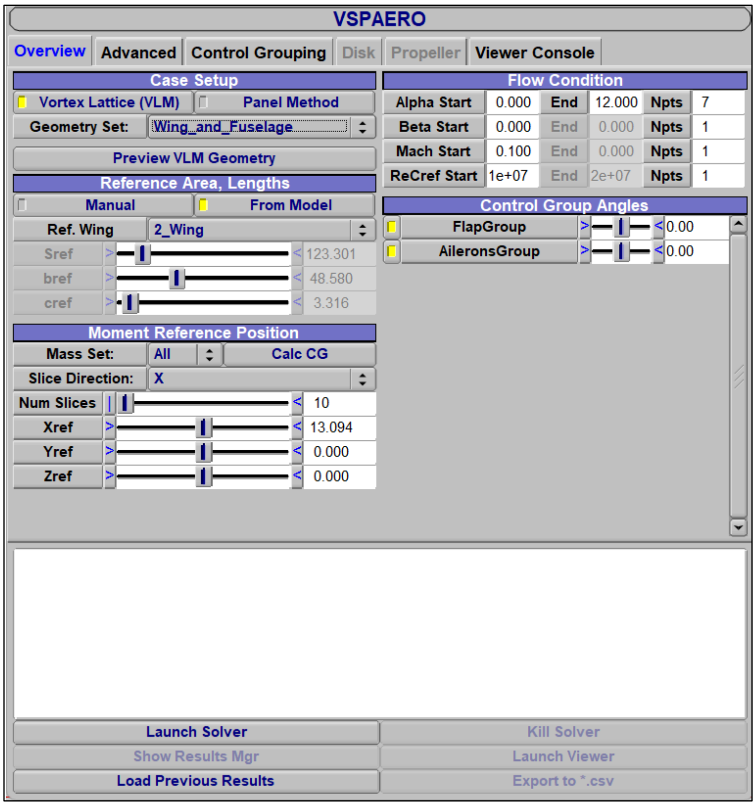

Vortex Lattice (VLM) ☑ Panel Method ☐
Geometry Set: Wing_and_Fuselage
Manual ☐ From Model ☑
Ref. Wing: 2_Wing
Sref 123.301
bref 48.580
cref 3.316
Mass Set: All
Slice Direction: X
Num Slices 10
Xref 13.094
Yref 0.000
Zref 0.000
Alpha Start 0.000 End 12.000 Npts 7
Beta Start 0.000 End 0.000 Npts 1
Mach Start 0.100 End 0.000 Npts 1
ReCref Start 1e+07 End 2e+07 Npts 1
FlapGroup 0.00
AileronsGroup 0.00

Figure 4.1 – VSPAERO’s interface

4.1.4 Control surfaces in VSPAERO

The Flaps and Ailerons have been organized in the control grouping window of VSPAERO (Figure 4.2).

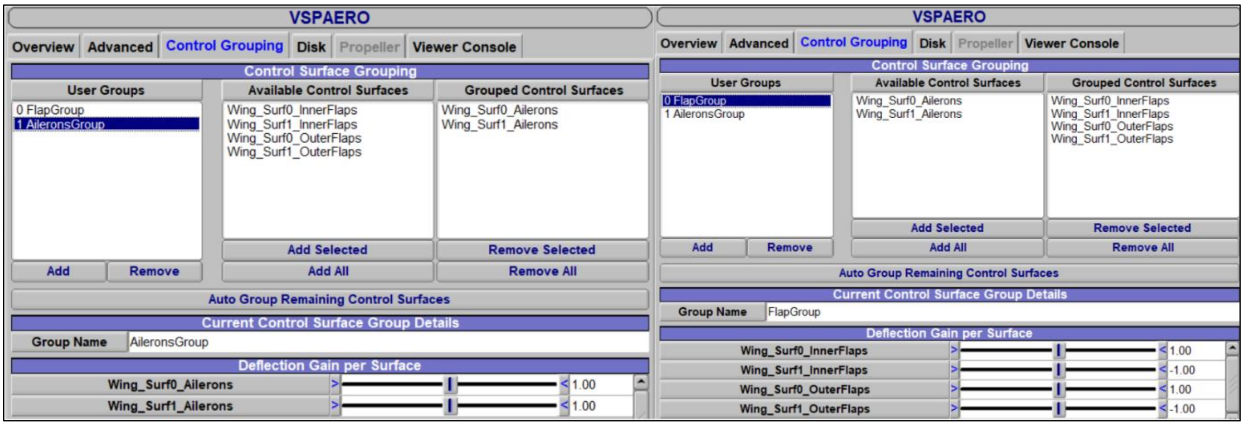

User Groups: 0 FlapGroup, 1 AileronsGroup
Available Control Surfaces: Wing_Surf0_InnerFlaps, Wing_Surf1_InnerFlaps, Wing_Surf0_OuterFlaps, Wing_Surf1_OuterFlaps
Grouped Control Surfaces: Wing_Surf0_Ailerons, Wing_Surf1_Ailerons
Group Name: AileronsGroup
Wing_Surf0_Ailerons 1.00
Wing_Surf1_Ailerons 1.00

User Groups: 0 FlapGroup, 1 AileronsGroup
Available Control Surfaces: Wing_Surf0_Ailerons, Wing_Surf1_Ailerons
Grouped Control Surfaces: Wing_Surf0_InnerFlaps, Wing_Surf1_InnerFlaps, Wing_Surf0_OuterFlaps, Wing_Surf1_OuterFlaps
Group Name: FlapGroup
Wing_Surf0_InnerFlaps 1.00
Wing_Surf1_InnerFlaps -1.00
Wing_Surf0_OuterFlaps 1.00
Wing_Surf1_OuterFlaps -1.00

Figure 4.2 – Control Grouping of VSPAERO

Both inner and outer flaps were included in the same group because only equal deflections for both components were considered in this analysis. For the left flaps, the deflection gain per surface was set to −1 because OpenVSP normally considers the control surfaces to deflect asymmetrically. A positive deflection of ailerons group means a clockwise roll seen from behind.

4.2 Clean Configuration Analysis

The first longitudinal analysis has been computed in a clean configuration, meaning without any deflection of the moving surfaces.

4.2.1 Lift and Wing Load

The results from VSPAERO has been reported in Table 4.1:

AoA	CL_W	CL_WR	CL_WF	CL_WFT	CD_W	CD_WR	CD_WF	CD_WFT
0	0.61	0.58	0.61	0.57	0.0171	0.0188	0.0170	0.0220
2	0.80	0.79	0.81	0.80	0.0244	0.0263	0.0251	0.0276
4	0.99	1.00	0.10	1.00	0.0337	0.0364	0.03423	0.0382
6	1.18	1.21	1.19	1.23	0.0452	0.0492	0.0463	0.0511
8	1.36	1.42	1.38	1.44	0.0585	0.0646	0.0588	0.0650
10	1.55	1.63	1.56	1.64	0.0738	0.0825	0.0744	0.0841
12	1.74	1.83	1.75	1.85	0.0907	0.1027	0.0921	0.1054

Table 4.1 – C_L and C_D values for clean configuration

As expected, C_L increases with α. Plotting these data we obtain the Figure 4.3.

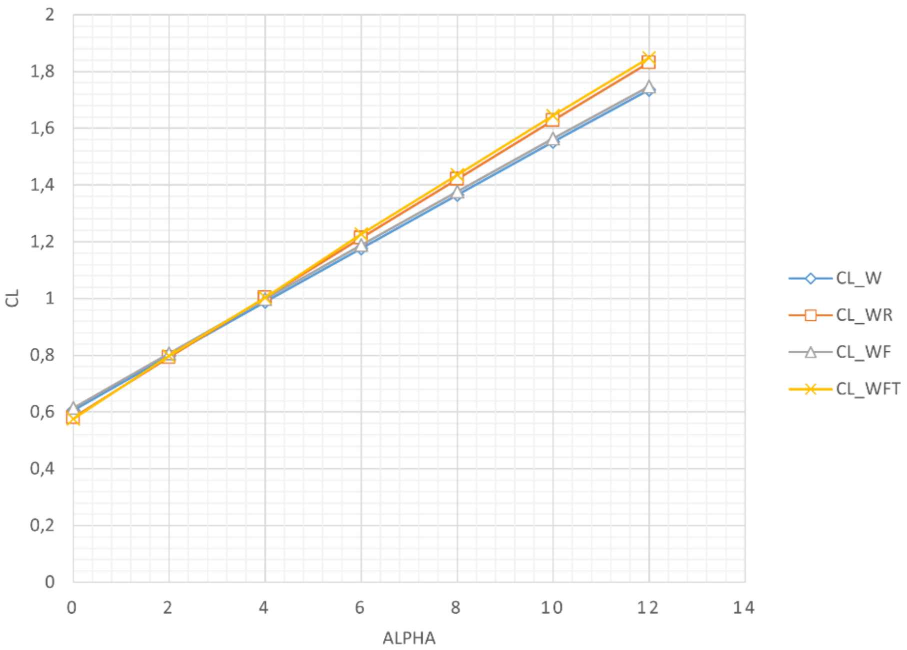

Figure 4.3 – C_L versus α chart for clean configuration

Figure 4.3 represents only the linear section of the lifting curve because VSPAERO cannot predict the stall due to the nature of the VLM. Adding the fuselage does not alter the lift. A negligible increase was attributed numerical round-off errors. Adding the ruddervator generates a very small decrease of C_L at low values of α due to the downwash from the wing that reaches the tail but only until α=4°. More important, the additional lifting surfaces increased the configuration lift curve slope, as expected. Also, a C_L versus C_D diagram can be plotted (Figure 4.4).

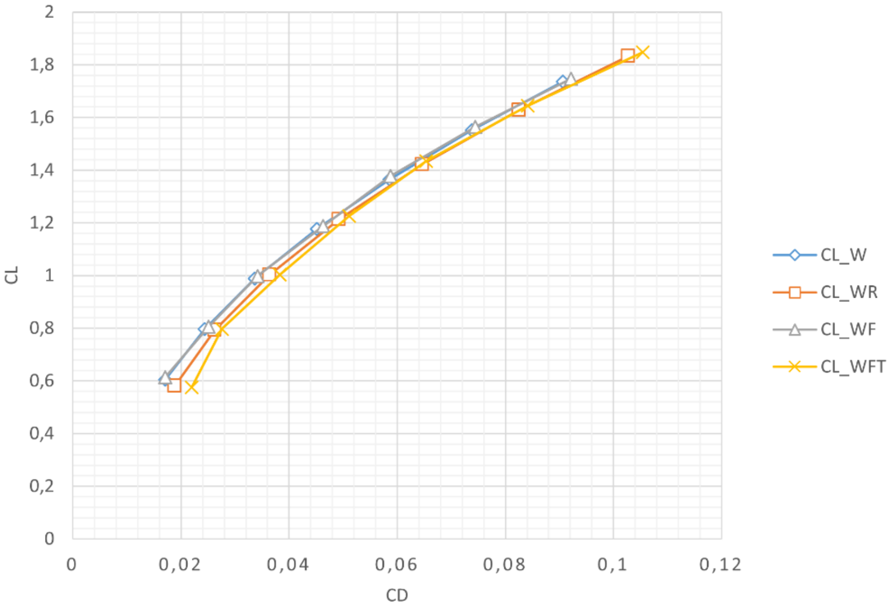

Figure 4.4 – C_L versus C_D chart for clean configuration

It is clear from the chart in Figure 4.4 that, as expected, adding components increases drag. With the slope function of Excel it is possible to compute the $C_{L\alpha}$ as the slope of the WFT's lift curve:

$$C_{L\alpha} = 0.10617\ deg^{-1} \tag{4.1}$$

Also is easy to extract the C_{L0}, the lift coefficient at α=0°:

$$C_{L0} = 0.57472 \tag{4.2}$$

In addition, the wing load diagram (Figure 4.5, Figure 4.6) can be plotted to see the effect of the α variation and of the fuselage. The y-axis is dimensionless respect the wingspan. Furthermore, opening the viewer in VSPAERO (Figure 4.7) allows to see the trailing wakes and the pressure distribution at every α.

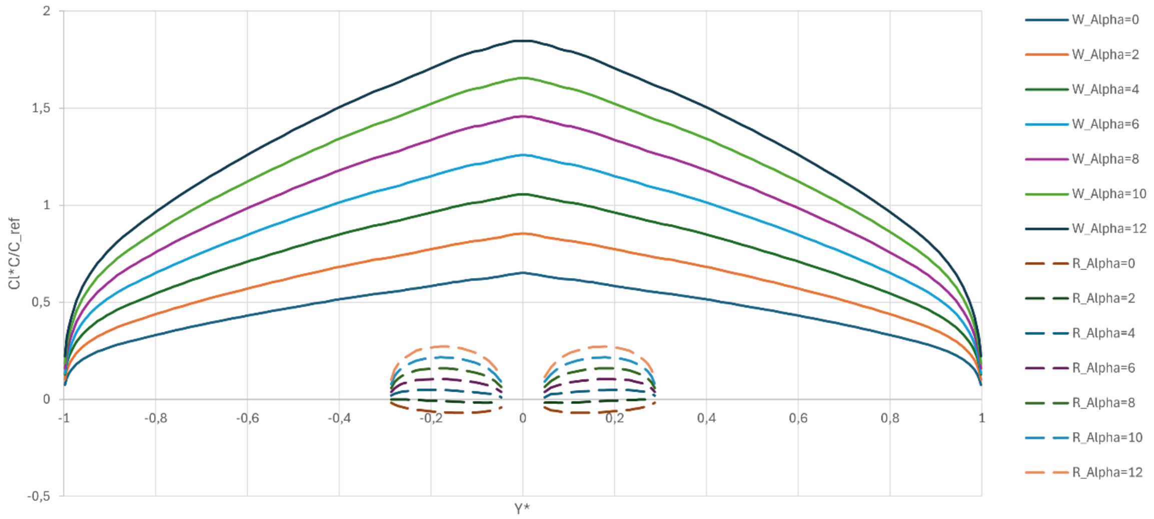

Figure 4.5 – Wing and tail load of WR set for different α and clean configuration

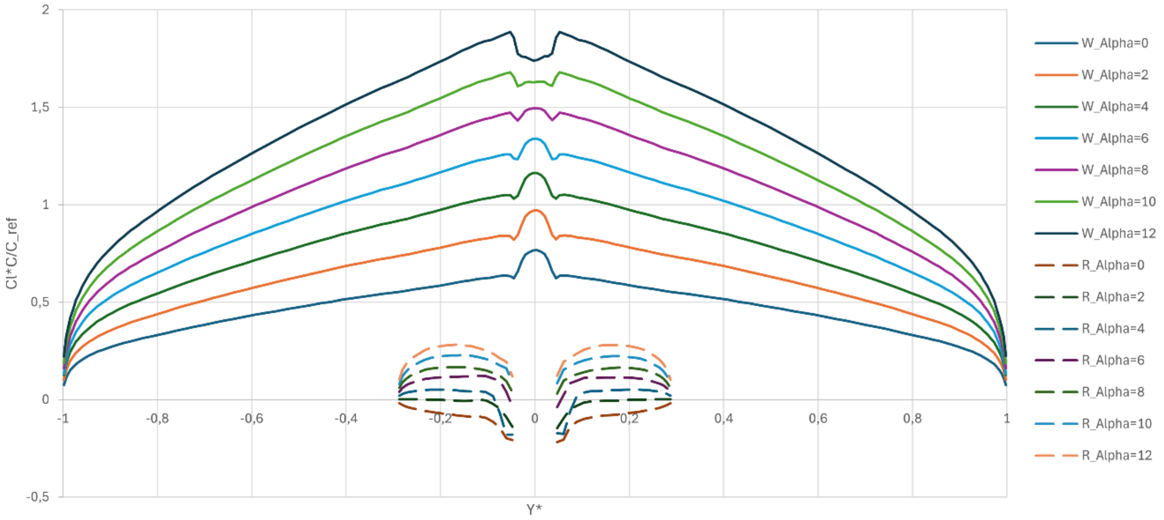

Figure 4.6 – Wing and tail load of WFT set for different α and clean configuration

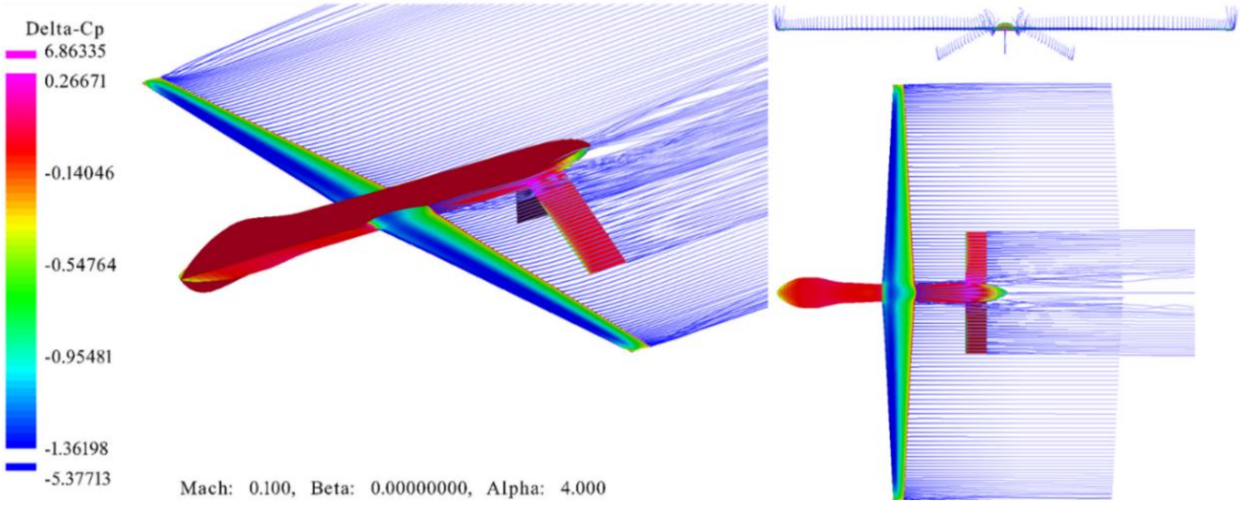

Figure 4.7 – Some views from the VSPAERO’s viewer

Moreover, in the VSPAERO viewer (Figure 4.8, Figure 4.9) the effect of the fuselage is noticeable from the shape of the trailing wake, due to the fact that the average fuselage surface is lower than the average wing surface, the trailing wakes at low angle of attack rotate around the fuselage, as they must by assumption always be tangent to the body, creating an additional downwash which increases the wing loading from α = 0° to α = 10° (Figure 4.8). From 10° onwards the trailing wakes remain above the average fuselage surface and are unable to encircle it, which decreases the downwash and the wing loading near the fuselage (Figure 4.9). At the same time this downwash reaches the tail and decrease the load on the tail behind the fuselage for α < 10°.

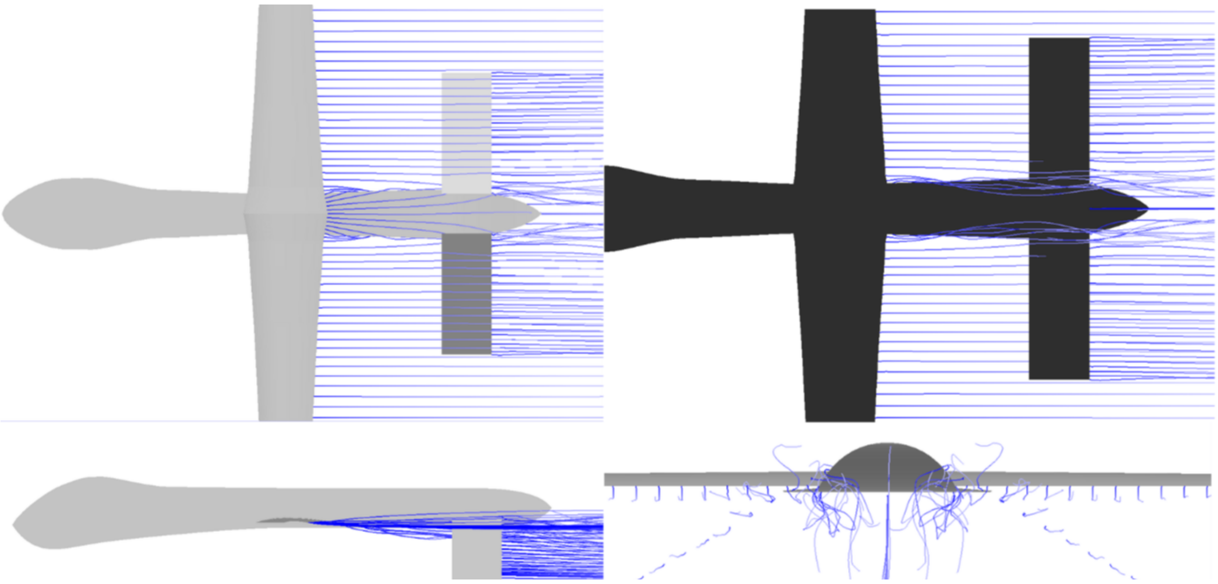

Figure 4.8 – Screenshots from the VSPAERO viewer at α=0°

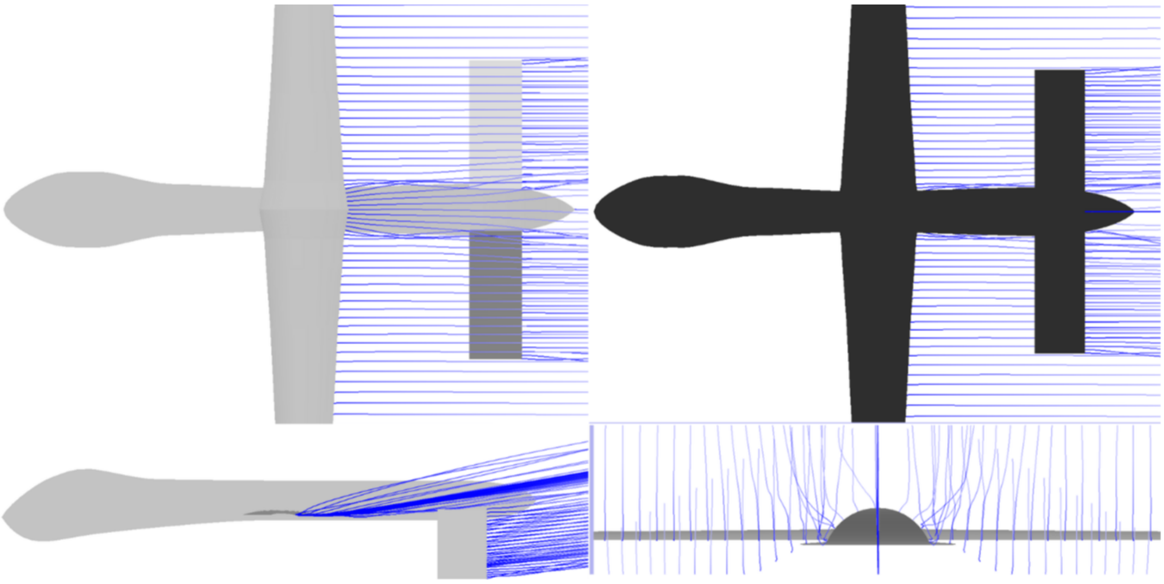

Figure 4.9 – Screenshots from the VSPAERO viewer at α=10°

4.2.2 Pitching Moment

Plotting the results in Table 4.2, the Figure 4.10 has been obtained.

AoA	CMy_W	CMy_WR	CMy_WF	CMy_WFT
0	-0.207	-0.146	-0.231	-0.129
2	-0.227	-0.218	-0.239	-0.222
4	-0.246	-0.289	-0.249	-0.269
6	-0.264	-0.357	-0.256	-0.355
8	-0.280	-0.424	-0.265	-0.407
10	-0.294	-0.489	-0.264	-0.461
12	-0.307	-0.551	-0.258	-0.505

Table 4.2 – C_{My} values for different α and clean configuration

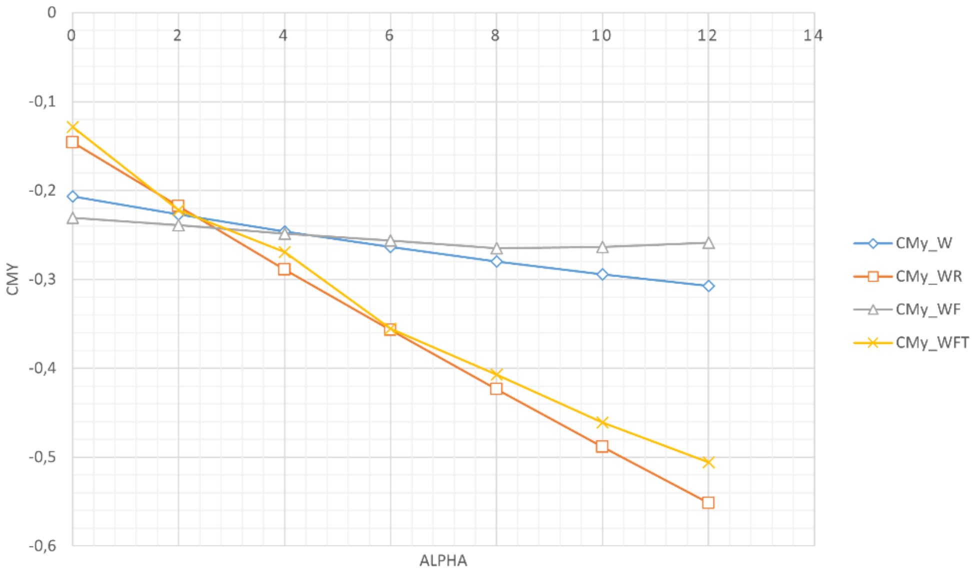

Figure 4.10 – C_{My} versus α chart for clean configuration

From Figure 4.10 it is noticeable that the fuselage decreases the slope, while the tail increases the aircraft stability increasing the curve slope, which is called also the derivative of longitudinal static stability, for the WFT set it values:

$$C_{M\alpha} = -0.0312\ deg^{-1} \tag{4.3}$$

From the equation:

$$C_{M\alpha} = C_{L\alpha}(\bar{X}_G - \bar{X}_N) \tag{4.4}$$

The coordinate of the neutral point and the SM can be obtained:

$$SM = (\bar{X}_G - \bar{X}_N) = \frac{C_{M\alpha}}{C_{L\alpha}} = \frac{-0.0312}{0.10617} = -0.29387 \tag{4.5}$$

$$\bar{X}_N = \bar{X}_G - SM = 0.3 + 0.29387 = 0.59387 \tag{4.6}$$

Thus, relative to the leading edge:

$$X_G = 0.3\bar{c} = 0.3 \cdot 3.31557 = 0.99467\ ft \tag{4.7}$$

$$X_N = \bar{X}_N \cdot \bar{c} = 0.59387 \cdot 3.31557 = 1.96902\ ft \tag{4.8}$$

The fact that the SM is negative confirms the RQ-1 static stability because the centre of gravity is placed ahead the neutral point. From the VSPAERO results it is also easy to extract the value of C_{My} at α = 0°:

$$C_{M0} = -0.12873 \tag{4.9}$$

4.2.3 *Efficiency*

Additionally, the lift and drag ratio, noted also as aerodynamic efficiency, has been plotted in Figure 4.11.

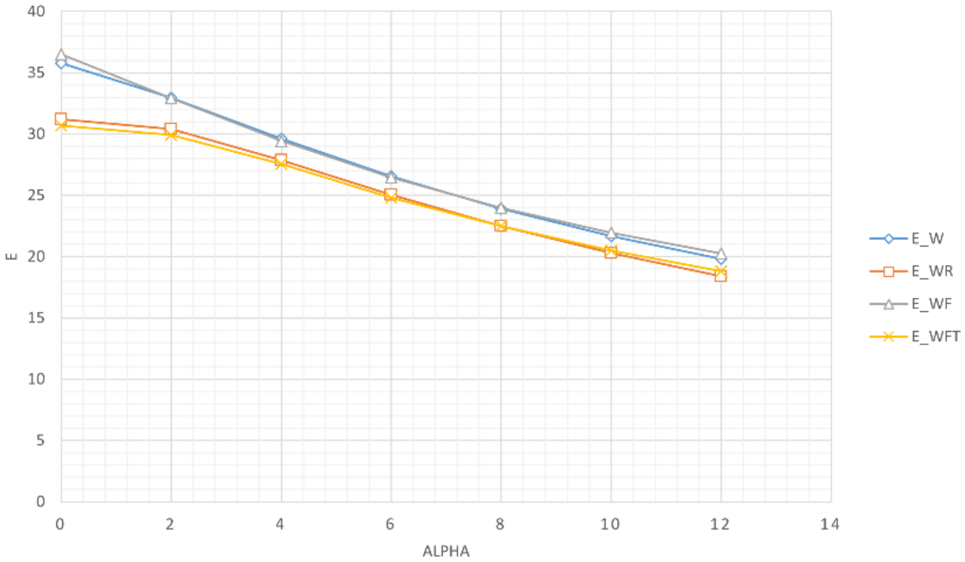

Figure 4.11 – Efficiency versus α chart for clean configuration

4.3 Flap effects on longitudinal aerodynamics

To evaluate the effect of a flap deflection δ_f the same analysis has been done but with a value of 0, 15, and 30 degrees for the FlapGroup deflection (Figure 4.2).

4.3.1 *Lift and Wing Load*

From the analysis on the WR and WFT set, charts in Figure 4.12 and Figure 4.13 have been obtained.

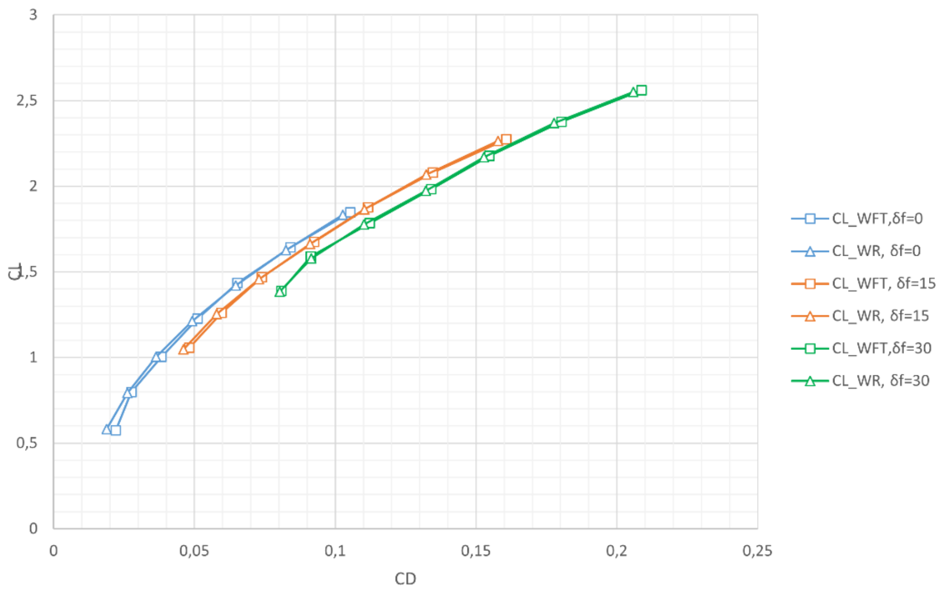

Figure 4.12 – C_L versus C_D chart for different δ_f values

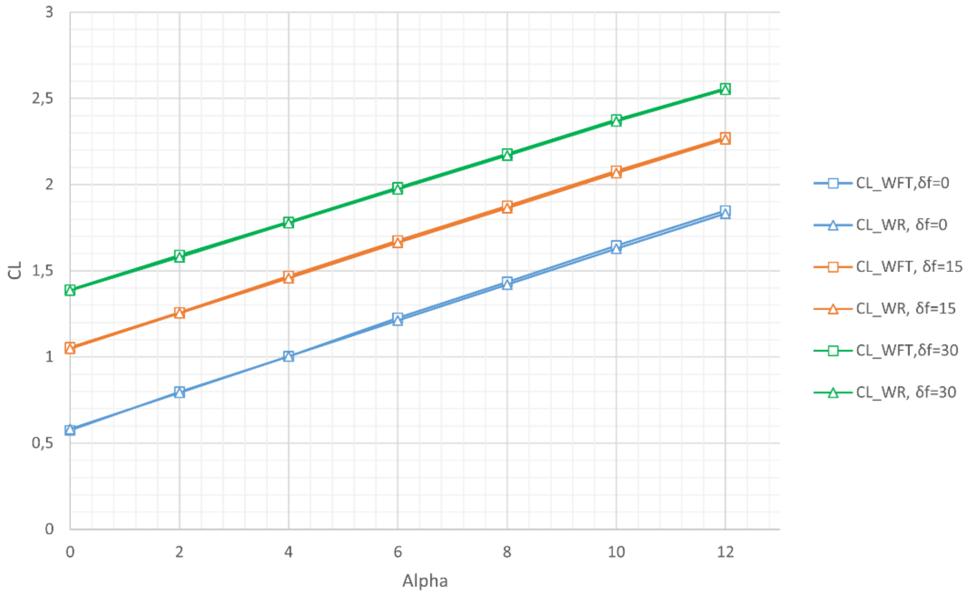

Figure 4.13 – C_L versus α chart for different δ_f values

As expected, both C_L and C_D increase deflecting the flaps. Collecting the data at α = 0°, the link between C_L and δ_f is highlighted in Table 4.3 and Figure 4.14.

δ_f	CL_WFT	CL_WR
0	0.57	0.58
15	1.06	1.05
30	1.39	1.38

Table 4.3 – C_L values for different δ_f

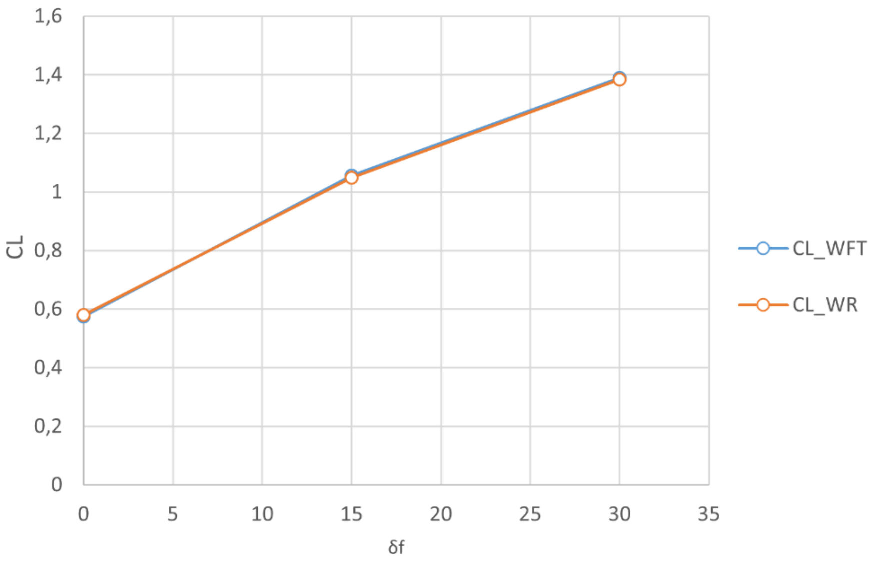

Figure 4.14 – C_L versus δ_f at α=0°

From this chart his possible to estimate the slope, which is the control derivative $C_{L\delta f}$:

$$C_{L\delta_f} = 0.02718\, deg^{-1} \tag{4.10}$$

Additionally, the wing and tail load can be plotted (Figure 4.15) to notice the effect of δ_f that causes the load to increase over the flaps and to become negative on the tail due to the downwash.

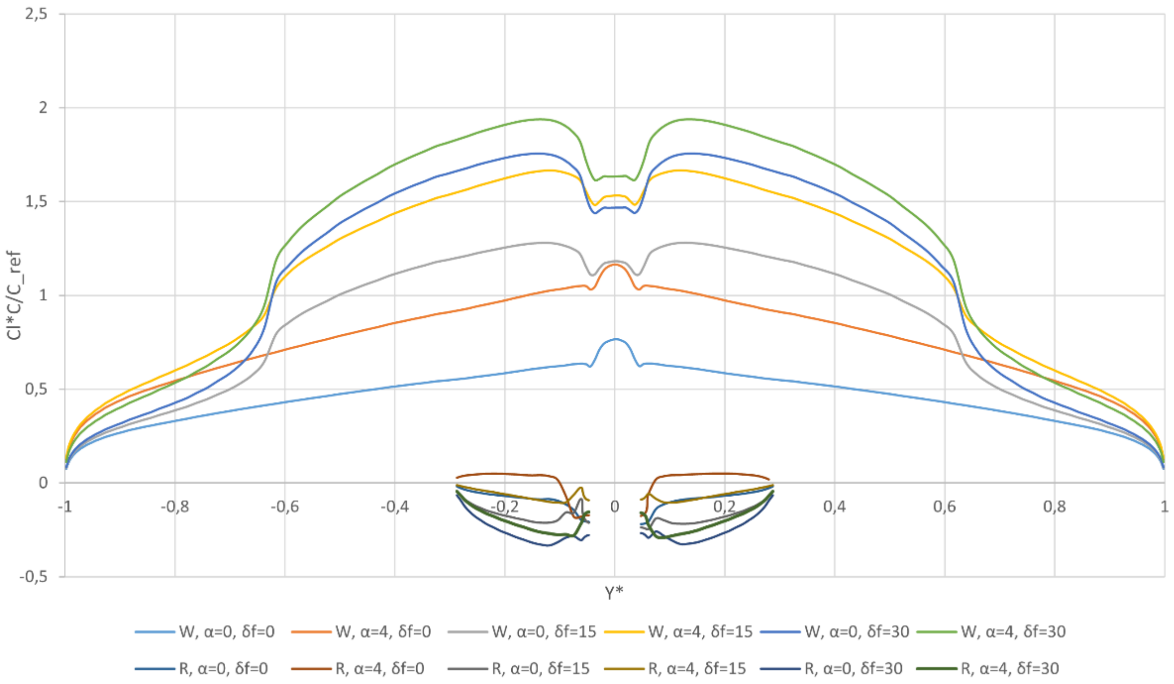

Figure 4.15 – Wing and tail load of WR set for different α and δ_f

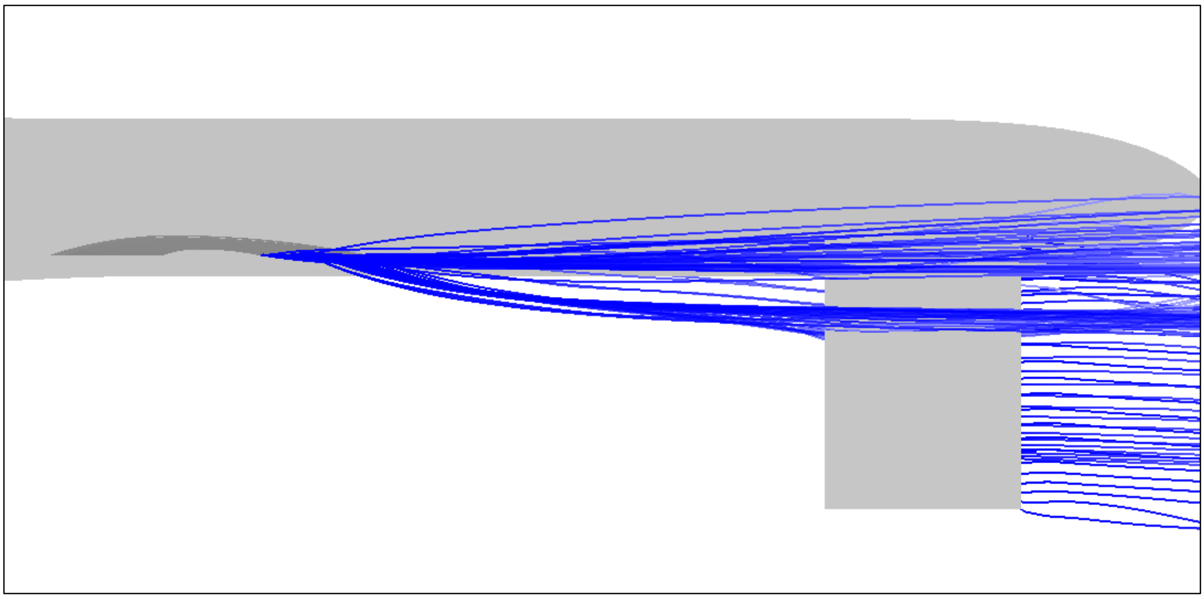

Figure 4.16 – VSPAERO viewer for α=0° and δ_f=30°

4.3.2 Pitching Moment

Also, the pitching moment coefficient is influenced by δ_f, as it can be seen from its values in Table 4.4 and from the charts in Figure 4.17 and Figure 4.18.

δ_f	CMy_WFT	CMy_WR
0	-0.129	-0.146
15	-0.196	-0.172
30	-0.205	-0.196

Table 4.4 – C_{My} values for different δ_f and α=0°

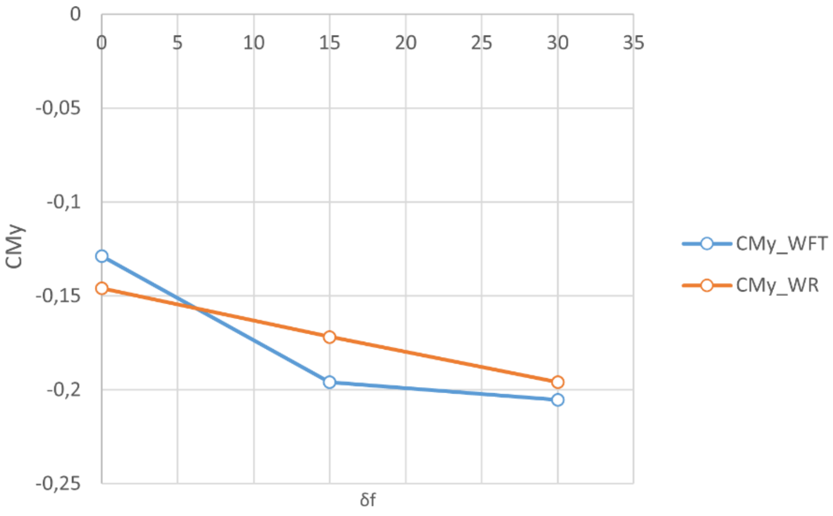

Figure 4.17 – C_{My} versus δ_f at α=0°

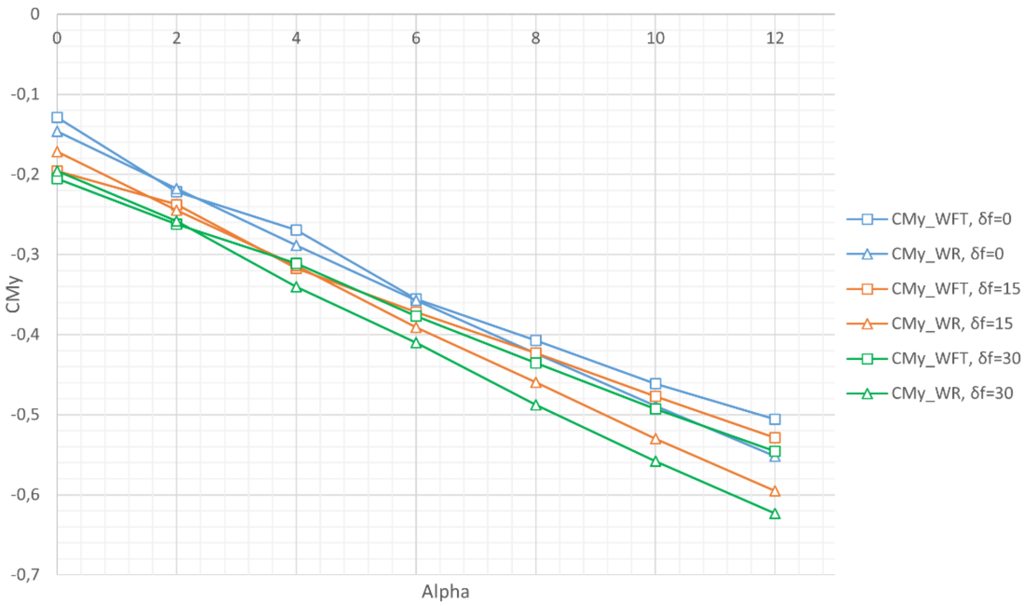

Figure 4.18 – C_{My} versus α chart for different δ_f values

From the Figure 4.17 is possible from evaluating the slope to find the control derivative:

$$C_{My\delta_f} = -0.00256\, deg^{-1} \tag{4.11}$$

So a δ_f generate an additional negative pitching moment because the aircraft's tendency to dive increases.

4.4 Ruddervator effects on longitudinal aerodynamics

As previously stated, when the ruddervator deflects symmetrically it works as an elevator. Thus, it is fundamental for longitudinal stability. The symmetrical deflection of the ruddervator is indicated with δ_e, which is positive if the trailing edge is deflected downward. To appreciate the effects of the ruddervators working as elevators, the analysis has been repeated changing in the user parameters (Figure 3.9) the δ_e value to 0, -5, -10, and -15 degrees.

4.4.1 Lift and Wing Load

From the results has been possible to plot the charts in Figure 4.19 and Figure 4.20. Clearly, increasing negatively δ_e, C_L decreases while C_D increases, even if the highest C_D is at $\delta_e = 0°$ due to the higher induced drag at larger C_L values.

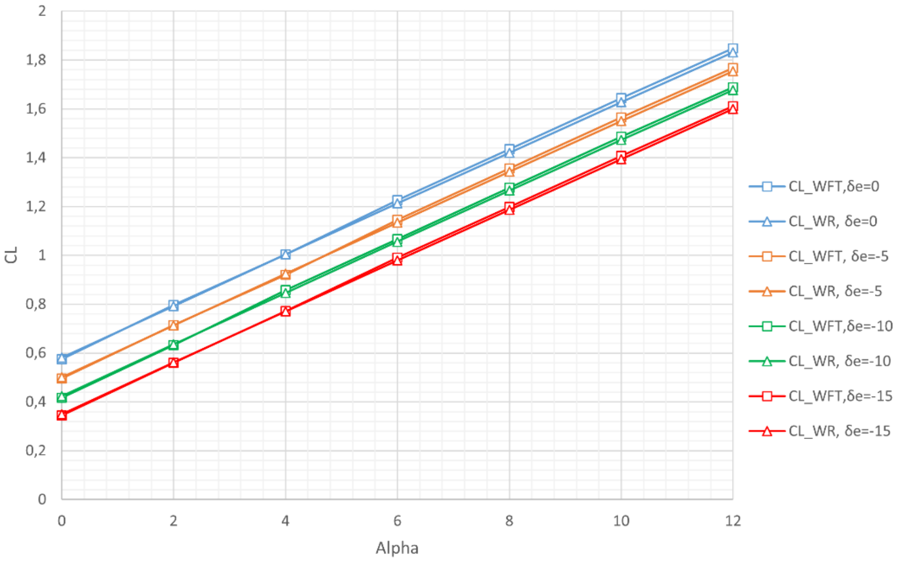

Figure 4.19 – C_L versus α chart for different δ_e values

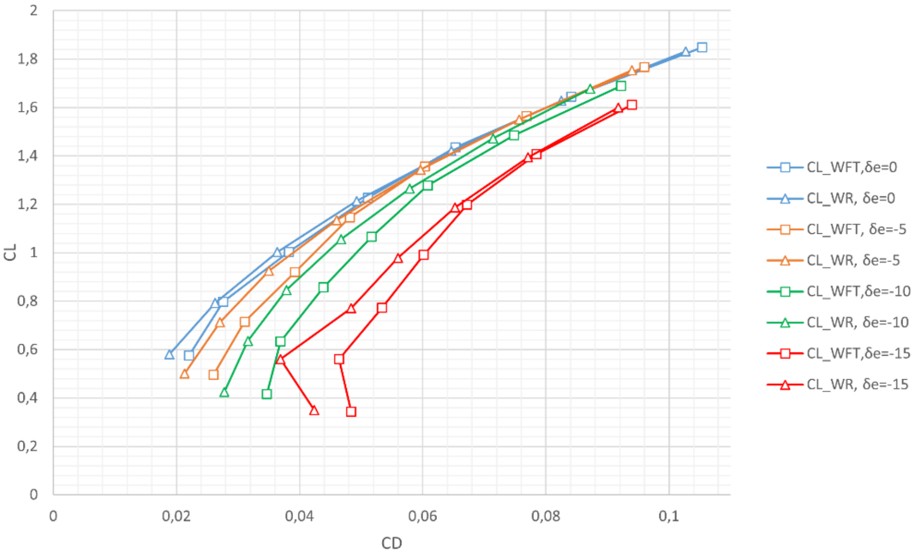

Figure 4.20 – C_L versus C_D chart for different δ_e values

Setting α=0°, it is possible to get the influence of δ_e on C_L (Table 4.5, Figure 4.21). By computing the slope, it is possible to find the $C_{L\delta e}$ which as expected is positive:

$$C_{L\delta_e} = 0.01542\ deg^{-1} \tag{4.12}$$

δ_e	AoA	CL_WR	CL_WFT
0	0	0.58	0.57
-5	0	0.50	0.50
-10	0	0.42	0.42
-15	0	0.35	0.34

Table 4.5 – C_L values at different δ_e

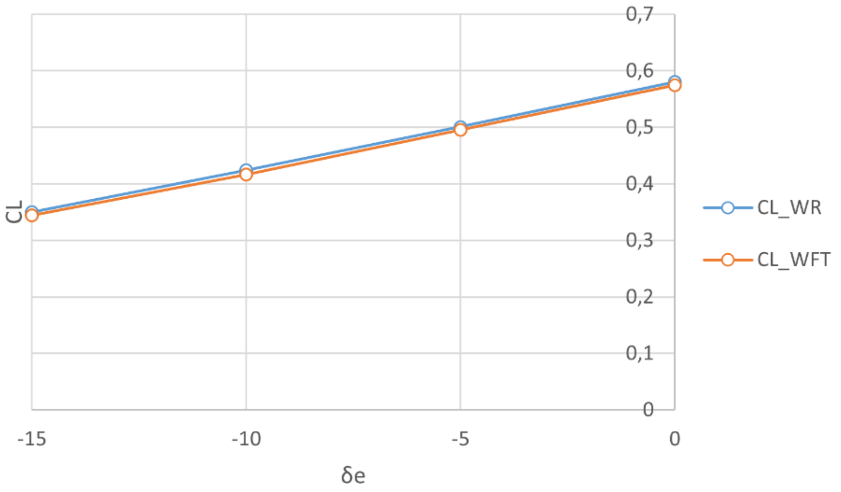

Figure 4.21 – C_L versus δ_e at α=0°

Regarding the wing and tail load (Figure 4.22), changing δ_e does not influence the load on the wing but decreases the load on the ruddervator.

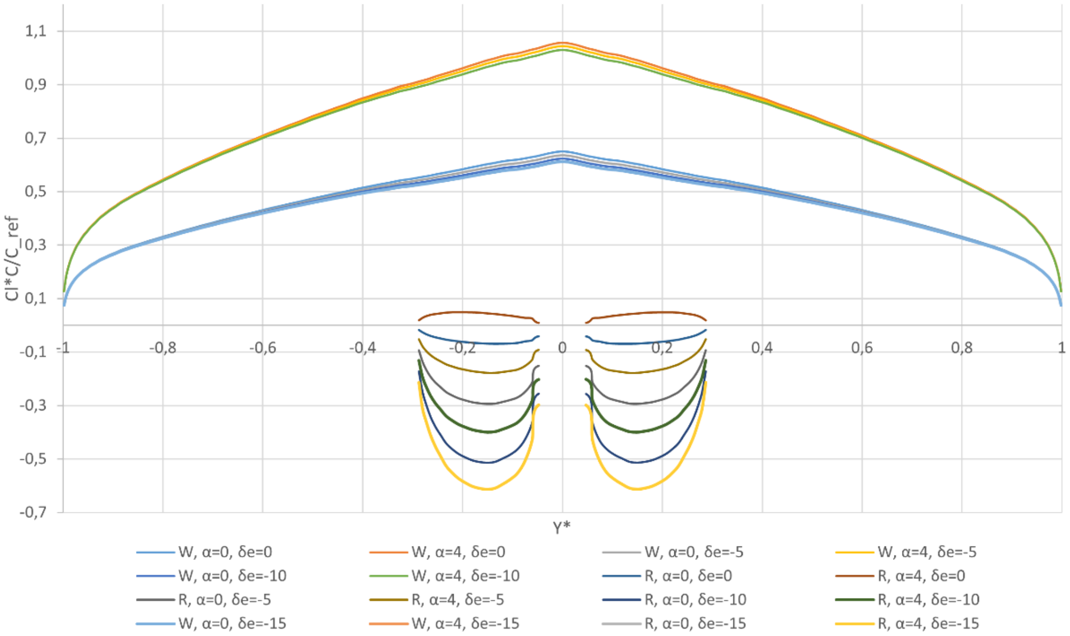

Figure 4.22 – Wing and tail load of WR set for different α and δ_e

4.4.2 Pitching Moment

Regarding the pitching moment, the results are shown in Figure 4.23, Table 4.6 and Figure 4.24. Predictability, C_{My} decreases with δ_e maintaining the same slope relative to α.

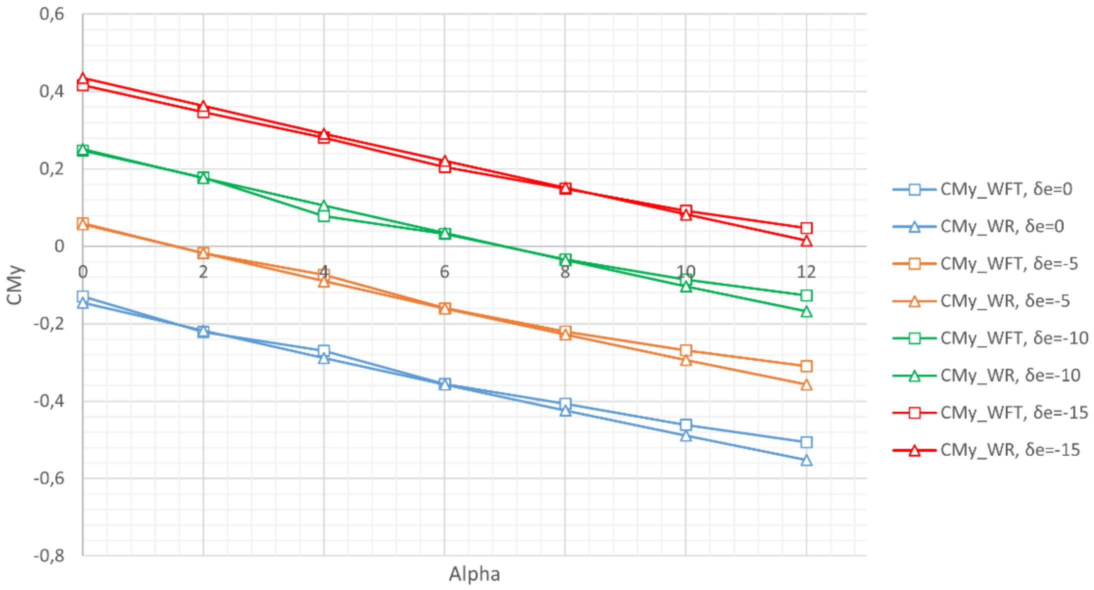

Figure 4.23 – C_{My} versus α chart for different δ_e values

δe	AoA	CMy_WFT	CMy_WR
0	0	-0.129	-0.146
-5	0	0.060	0.057
-10	0	0.248	0.252
-15	0	0.417	0.436

Table 4.6 – C_{My} values for different δ_e

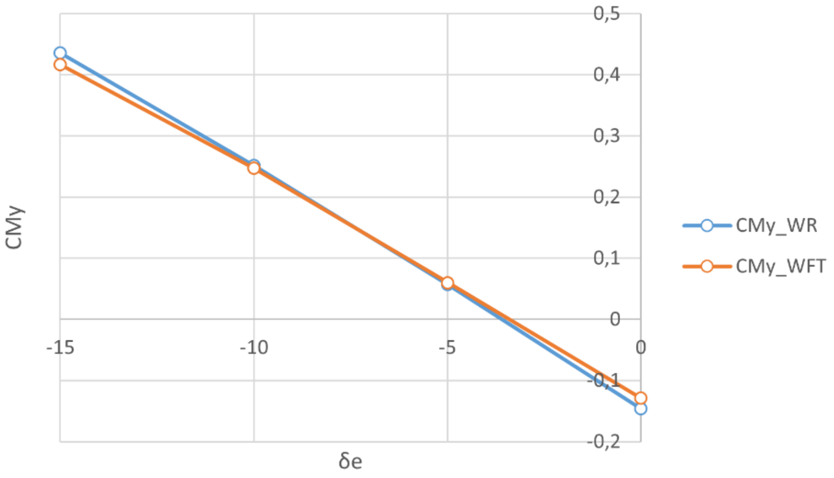

Figure 4.24 – C_{My} versus δ_e at α=0

Evaluating the slope is possible to extract the value of the control derivative $C_{My\delta e}$:

$$C_{My\delta_e} = -0.03649\ deg^{-1} \tag{4.13}$$

It represents the longitudinal control's power of the ruddervator.

4.4.3 C_L trim values

With the data collected it has been possible to compute the C_L trim values, which are the C_L values when the total pitching moment is zero at the δ_e given. First of all, the pitching moment's equilibrium was imposed to find the α trim values:

$$C_M = C_{M0(\delta_e)} + C_{M\alpha}\cdot\alpha = C_{M0(\delta_e=0)} + C_{M\alpha}\cdot\alpha + C_{M\delta_e}\cdot\delta_e = 0 \tag{4.14}$$

$$\alpha_T = \frac{-C_{M0(\delta_e=0)} - C_{M\delta_e}\cdot\delta_e}{C_{M\alpha}} \tag{4.15}$$

Then with these chosen values of α_T and δ_e, the values of C_{LT} have been found (Table 4.7):

$$C_{L_T} = C_{L0(\delta_e=0)} + C_{L\alpha}\cdot\alpha_T + C_{L\delta_e}\cdot\delta_e \tag{4.16}$$

δ_e	α trim	C_L trim
0	-4.13	0.14
-5	1.72	0.68
-10	7.57	1.22
-15	13.42	1.77

Table 4.7 – The values of α_T and C_{LT} computed

These values can be plotted together with the other curves in Figure 4.25.

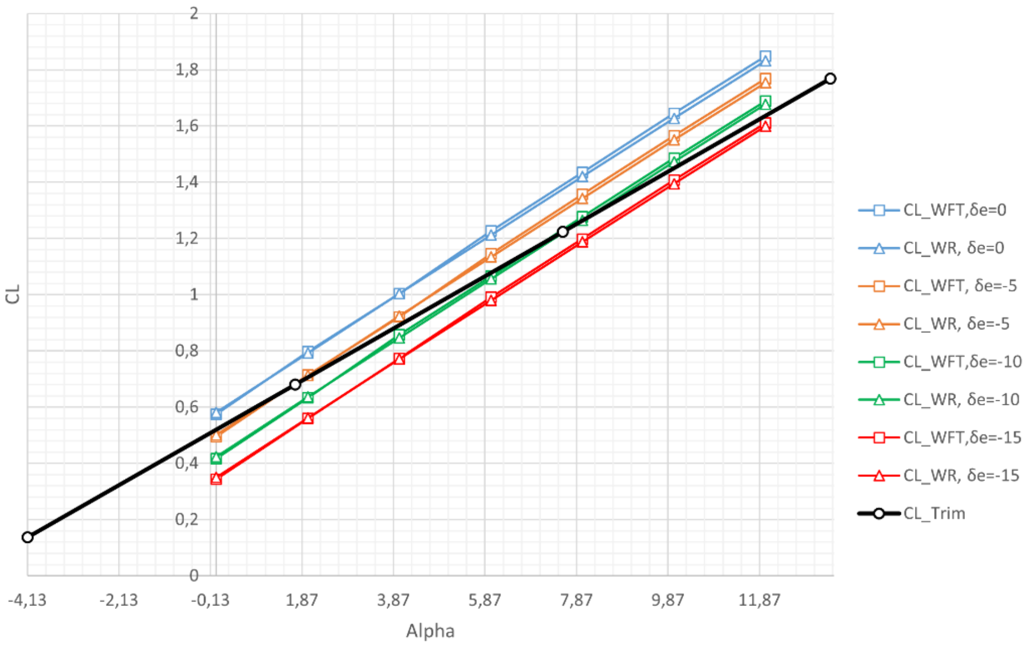

Figure 4.25 – C_L versus α chart for different δ_e values and C_{LT} versus α_T

From Figure 4.25 is noticeable that the slope of the trimmed curve is smaller than the slope of the other curves. The lift equilibrium curve is the representation of this equation:

$$C_{L_E} = C_{L0_E} + C_{L\alpha_E} \cdot \alpha_T(\delta_e) \tag{4.17}$$

Where C_{LE} indicates the values of C_L, depending on α, when the ruddervators are deflected so that the total pitching moment of the aircraft is zero. With the slope and intercept functions in Excel these values have been found:

$$C_{L0_E} = 0.52032 \tag{4.18}$$

$$C_{L\alpha_E} = 0.09299\ deg^{-1} \tag{4.19}$$

It can be seen that the $C_{L\alpha E}$ is smaller than the $C_{L\alpha}$ previously computed (Equation 4.1). Additionally, in Figure 4.26 δ_e versus $C_{L\alpha E}$ has been plotted.

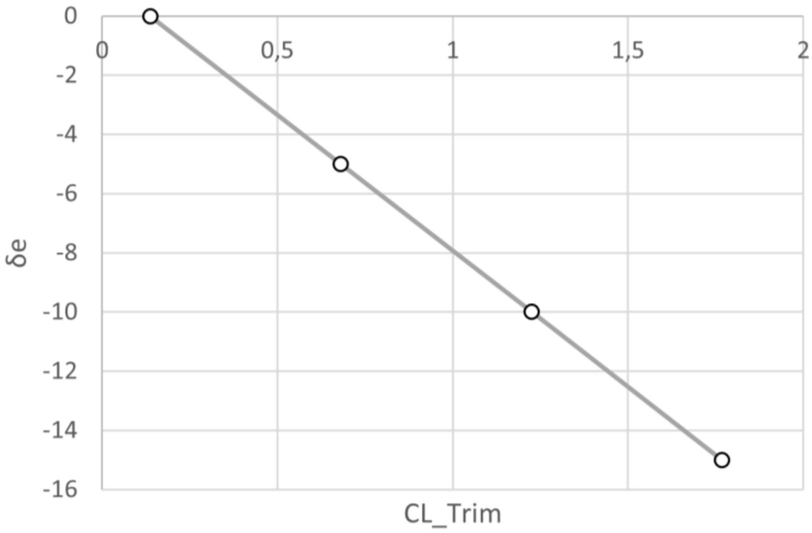

Figure 4.26 – δ_e versus $C_{L\alpha E}$

5. Lateral Directional Aerodynamic Analysis

5.1 VSPAERO parameters

5.1.1 Flow conditions

The VSPAERO parameters are the same as the longitudinal analysis except that this time the analysis was done by varying the sideslip angle β, for 3 different values of α. Precisely the flow conditions chosen (Figure 5.1) are:

- A Mach number equal to 0.1;
- A Reynolds number of 10 million;
- A set of values of β from -6 degrees to 20 degrees, with a step of 2 degrees, so 14 points overall.
- An α angle of values 0, 5, and 10 degrees, so 3 points.

This analysis has been focused on:

- the rolling moment coefficient C_{Mx};
- the yawing moment coefficient C_{Mz};
- and the sideforce coefficient C_{Fy}.

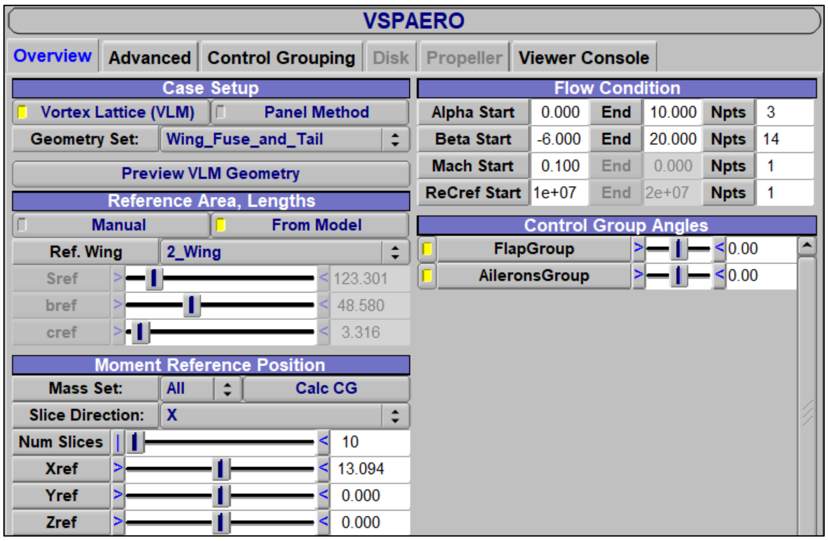

● Vortex Lattice (VLM) ○ Panel Method
Geometry Set: Wing_Fuse_and_Tail
○ Manual ● From Model
Ref. Wing: 2_Wing
Sref: 123.301
bref: 48.580
cref: 3.316
Mass Set: All
Slice Direction: X
Num Slices: 10
Xref: 13.094
Yref: 0.000
Zref: 0.000

	Start	End	Npts
Alpha	0.000	10.000	3
Beta	-6.000	20.000	14
Mach	0.100	0.000	1
ReCref	1e+07	2e+07	1

FlapGroup: 0.00
AileronsGroup: 0.00

Figure 5.1 – VSPAERO parameters for lateral directional analysis

5.1.2 OpenVSP Reference System

OpenVSP considers moments positive in the anti-clockwise direction relative to its reference axes, in particular, in relation to the fuselage, the Z axis is directed upwards and the X axis backwards. The positive direction of the moments is highlighted in Figure 5.2.

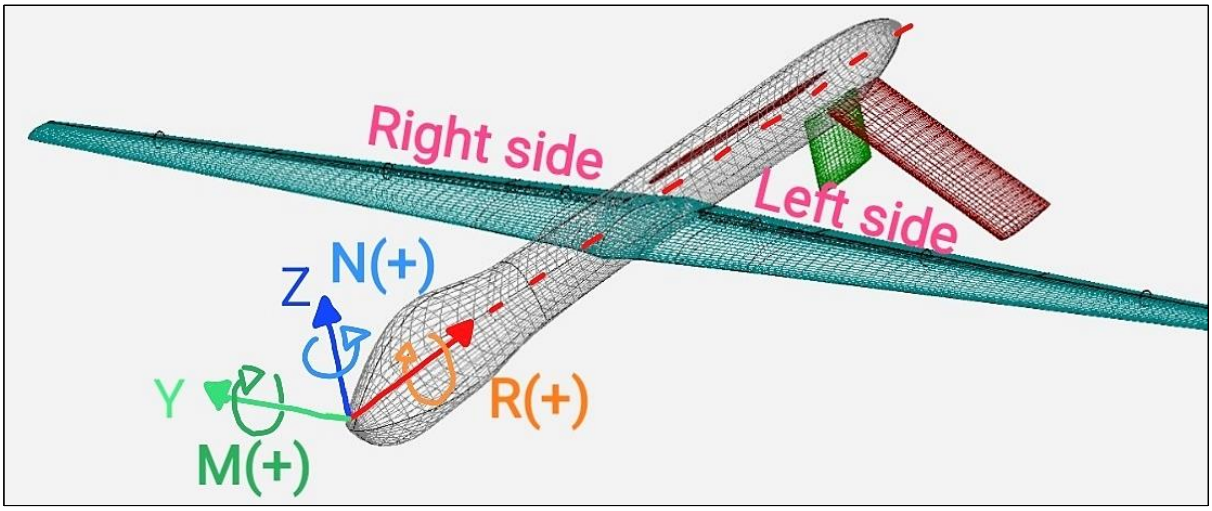

Figure 5.2 – Positive directions of moments in the OpenVSP reference system

5.2 Clean Configuration Analysis

5.2.1 Lift and Drag Coefficients

The charts obtained are shown in Figure 5.3. From the chart, it is clear that in cruise conditions, at small α, there is no significant change in C_L with β.

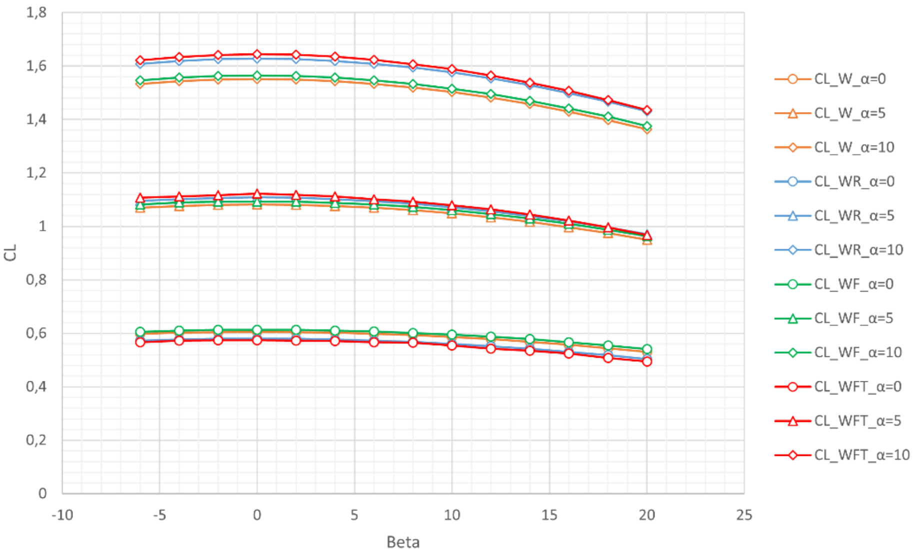

Figure 5.3 – C_L versus β chart for different α values

5.2.2 *Wing Load*

The load has been analysed in the case α=0° for the WFT set in Figure 5.4, where the red arrows indicate the direction of the increasing β angle.

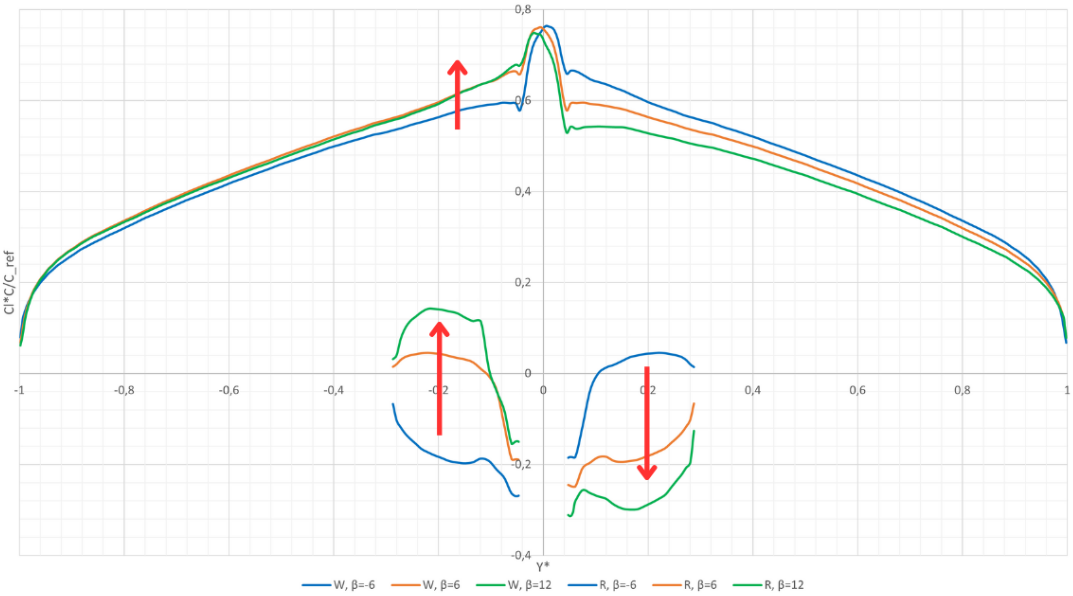

Figure 5.4 – Wing and tail load of WFT set for different β

From the results shown in Figure 5.4 is understandable that increasing β shifts the load rise on the left side of the wing due to the fuselage and at higher β the decline on the right side increases. Meanwhile, on the tail, the negative dihedral angle causes the left ruddervator to see a higher angle of attack than the right one, which therefore generates less lift (Figure 5.5).

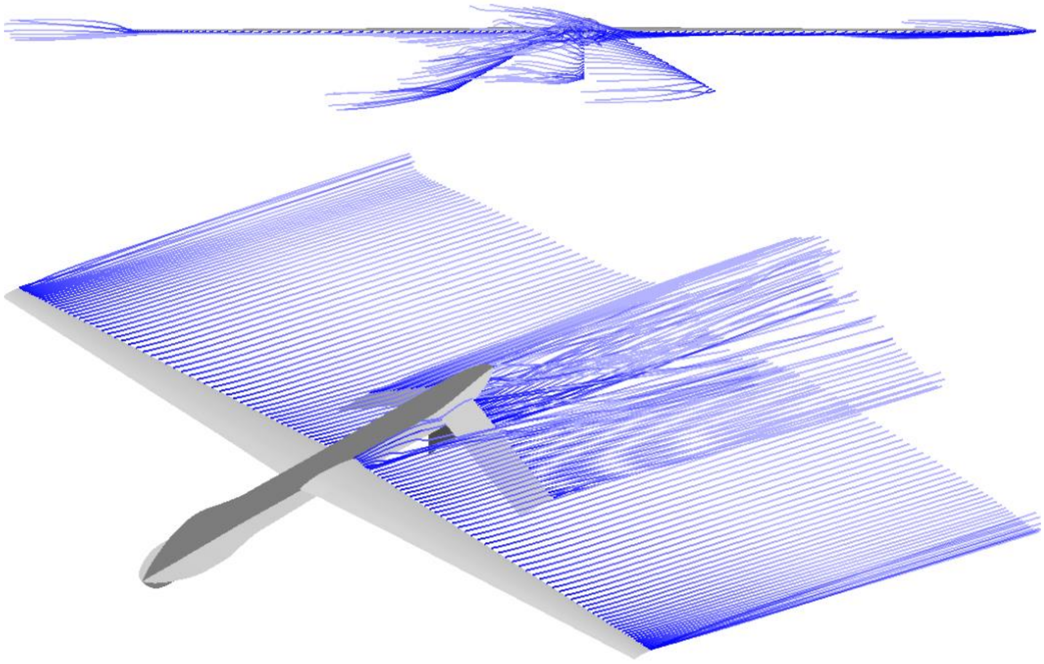

Figure 5.5 – VSPAERO viewer for α=0° and β=16°

This behaviour suggests that the tail for his negative dihedral angle induces roll instability generating a negative rolling moment for β > 0°, according to the OpenVSP reference system.

5.2.3 Rolling Moment

As foreseen exanimating the load chart, the aircraft has a negative rolling moment for β>0° that became stronger increasing β. The results in Figure 5.6 show an unstable behaviour, because to have stability, according to OpenVSP reference system, the aircraft should have an increasing rolling moment with β, so a positive roll stability derivative $C_{Mx\beta}$, instead from the results its value is:

$$C_{Mx_\beta} = -0.00107\ deg^{-1} \tag{5.1}$$

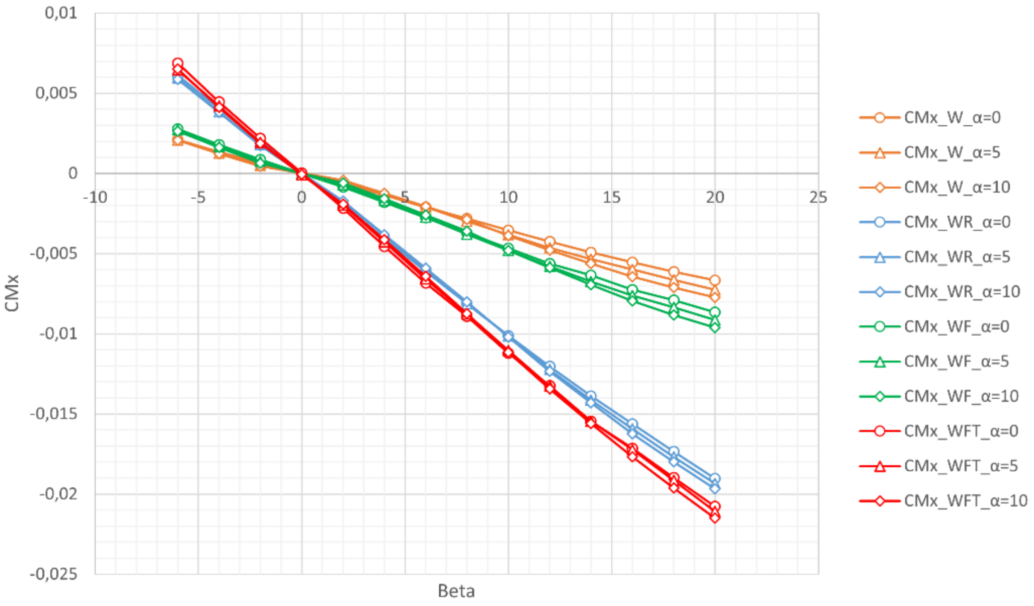

Figure 5.6 – Rolling moment coefficient C_{Mx} versus β at different α

A negative $C_{Mx\beta}$ is inconvenient for stability and it can cause the wing skid phenomenon, but in some rare cases, it can be useful to increase the manoeuvrability of aircraft, usually for military combat ones. From the chart can be seen that every component has this instability and the biggest contribute is given by the ruddervator, due to his negative dihedral angle. This was foreseeable because of certain geometric features of the aircraft that contribute to roll instability, such as the low mounted wing, the negative dihedral angle of the ruddervator and the absence of a wing's sweep angle. The aircraft probably features an automatic stability and control system that deflects the ailerons to counteract this negative rolling moment derivative.

5.2.4 Sideforce and Yawing Moment

The angle of sideslip β is considered positive when the flow arrives from the right side. To be stable the aircraft is expected to yaw towards the direction of the incoming flow. Thus, it should generate a negative sideforce and a negative yawing moment according to the OpenVSP reference system. From the results obtained (Figure 5.7, Figure 5.8) is noticeable that the main contributions to the C_{Fy} are related to the ruddervator and the vertical tailplane.

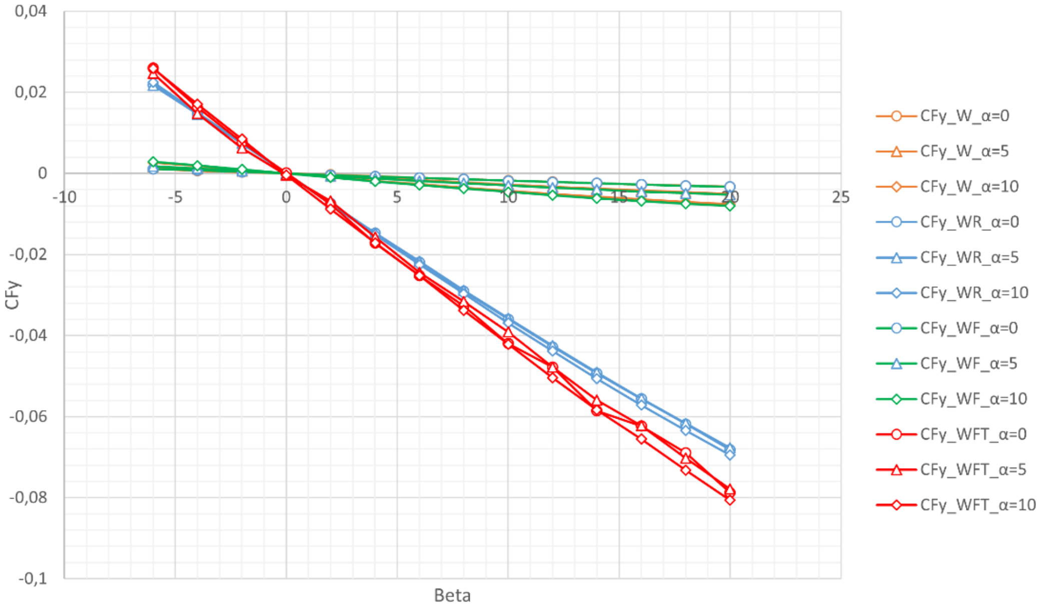

Figure 5.7 – Sideforce coefficient C_{Fy} versus β for different α values

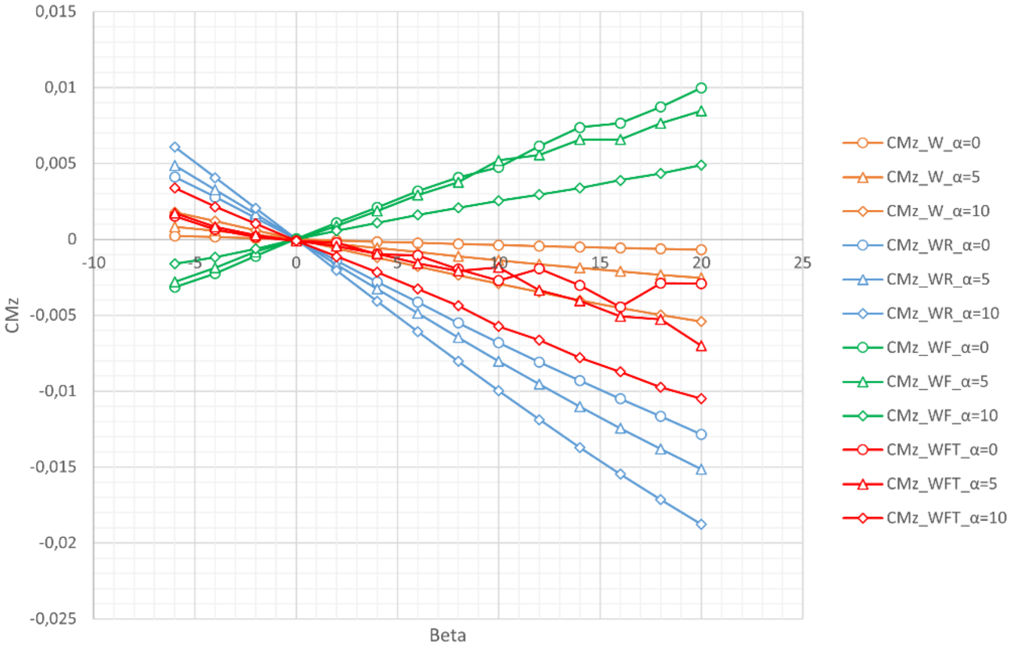

Figure 5.8 – Yawing moment coefficient C_{Mz} versus β for different α values

The ruddervator, as previously stated, generates two opposite aerodynamic forces on each half wing, because the negative dihedral angle causes the downwind half-wing to see a smaller angle of attack than the other. These two forces cancel each other out vertically but they combine horizontally to create a negative side force. The vertical tailplane is fixed, it is not a moving surface, but at β≠0° it works as a stabilizer because it sees an angle of attack, generating a horizontal lift, which contributes to the stabilizing yawing moment and side force. From the chart in Figure 5.8 can be seen that the fuselage has a destabilizing effect, while the ruddervator and the vertical tail, as stated, increase the yawing stability. Computing the slope of the WFT set at α=0°:

$$C_{Mz_\beta} = -0.00019\, deg^{-1} \tag{5.2}$$

As foreseen, the result is a negative yawing stability derivative.

5.3 Ailerons effects on lateral directional aerodynamics

To evaluate the ailerons effects on lateral directional aerodynamics the analyses have been done with the same flow conditions, for WR and WFT sets, but only at α=0° and with an ailerons' deflection δ_a of 0, 15, 30 degrees. The ailerons have been deflected using the control grouping tool of VSPAERO (Figure 4.2). A positive δ_a means that the right aileron is deflected downwards while the left upwards, so a positive rolling moment is generated (Figure 5.9).

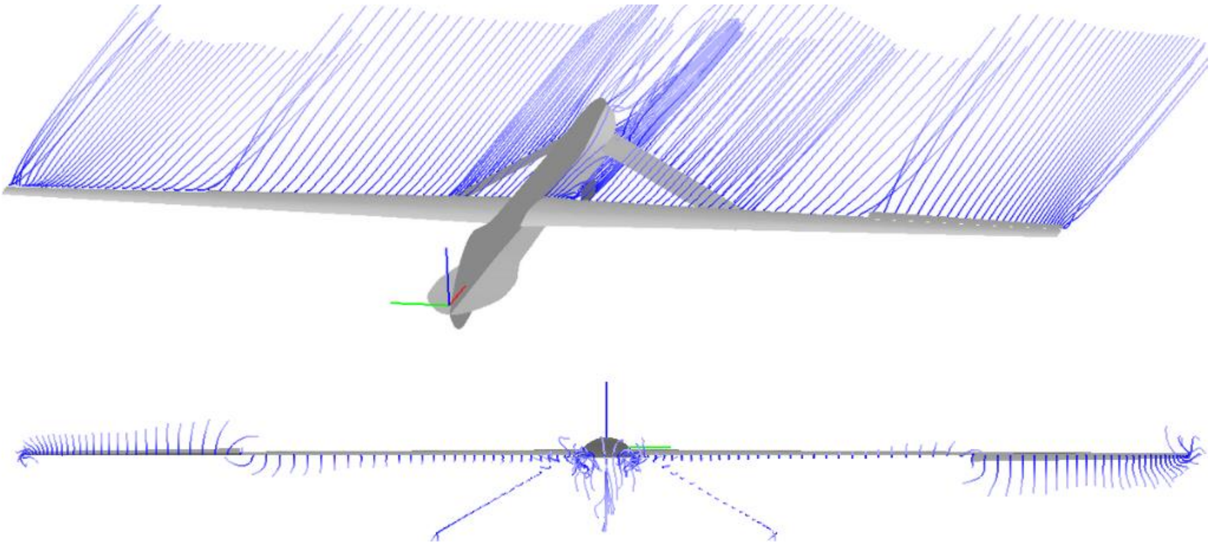

Figure 5.9 – Ailerons deflected of 30° in the VSPAERO viewer

5.3.1 *Wing and Tail Load*

From the load chart in Figure 5.10, it is evident the rise on the right aileron deflected downwards and the reduction on the left aileron deflected downwards. Meanwhile, the load on the tail is not influenced by δ_a.

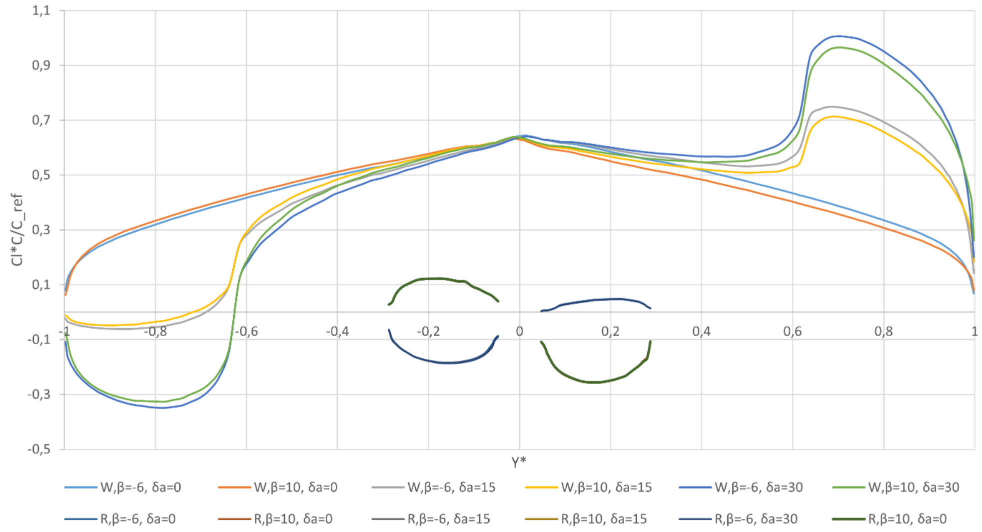

Figure 5.10 – Wing and tail load of WR set for different β and δ_a

5.3.2 *Rolling moment*

From the results shown in Figure 5.11, Figure 5.12 and Table 5.1, as expected, a positive δ_a generates a positive contribute that increases C_{Mx}, which maintains a negative slope that results in roll instability. The control derivative can be computed from the slope of the C_{Mx} versus δ_a curve of WFT set in Figure 5.12. The result is:

$$C_{Mx\delta_a} = 0.00421\ deg^{-1} \tag{5.3}$$

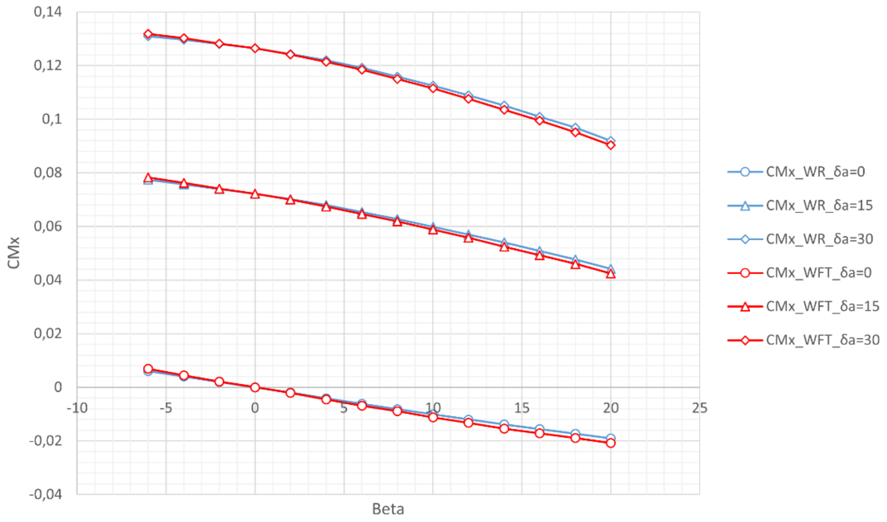

Figure 5.11 – C_{Mx} versus β at different δ_a

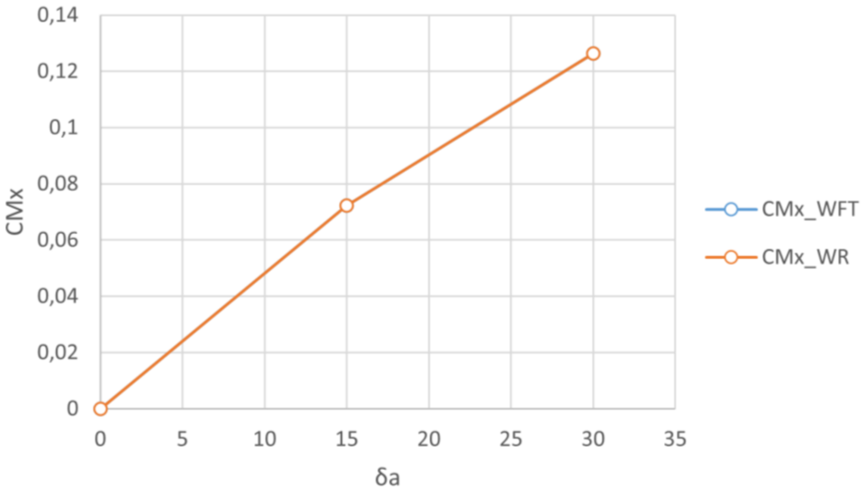

Figure 5.12 – C_{Mx} versus δ_a

δa	Beta	CMx_WR	CMx_WFT
0	0	1.57E-05	1.57E-05
15	0	7.22E-02	7.22E-02
30	0	1.26E-01	1.26E-01

Table 5.1 – C_{Mx} values for different δ_a

5.3.3 Sideforce and Yawing Moment

The sideforce coefficent in Figure 5.13 remain almost the same chainging δ_a. Instead, the yawing moment cofficent (Figure 5.14) decreases for positive δ_a, because, when the deflection is perfectly asymmetrical, the aileron deflected downwards on the right wing generates a greater aerodynamic force than the left side, hence generating a larger induced drag. This causes an adverse yaw to the right, which must be countered by an asymmetrical ruddervator deflection.

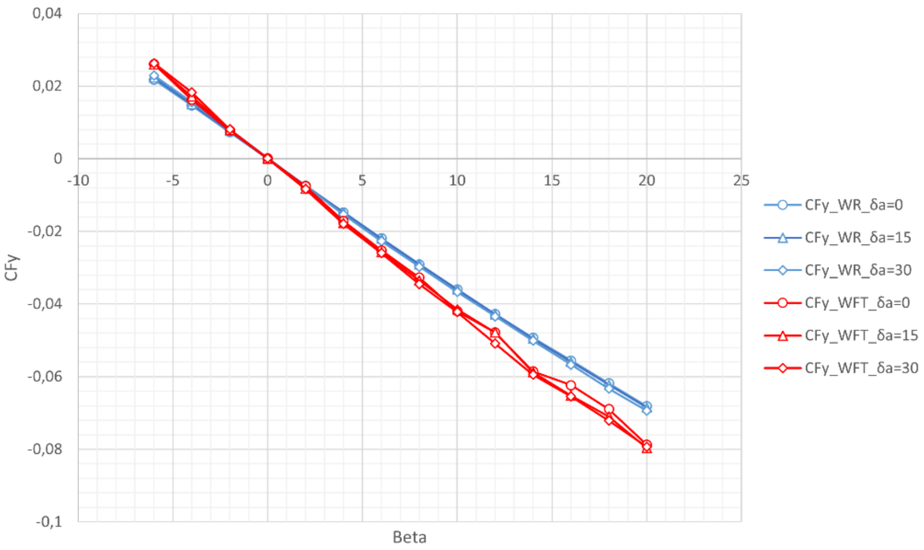

Figure 5.13 – C_{Fy} versus β at different δ_a

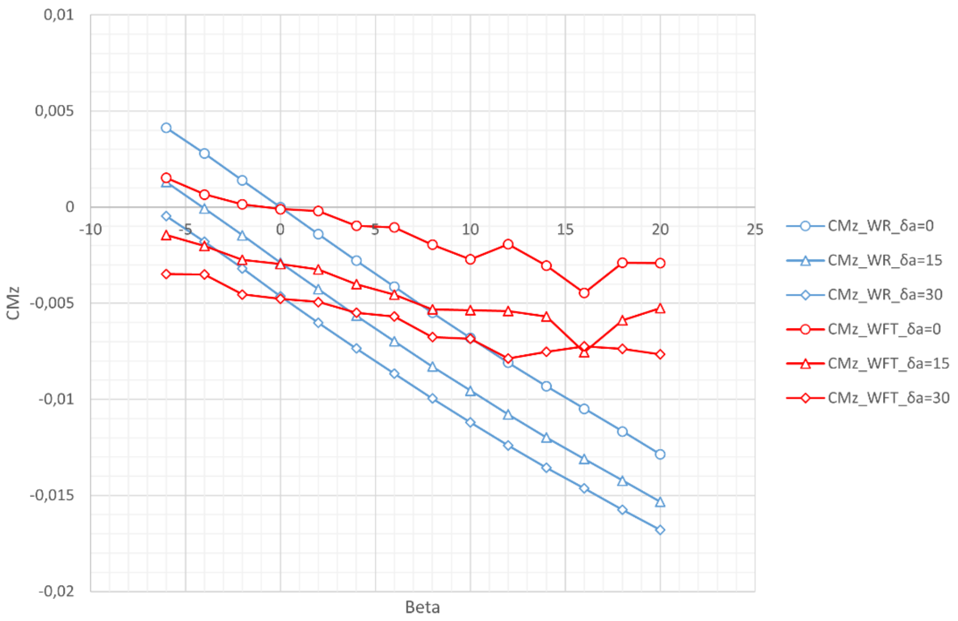

Figure 5.14 – C_{Mz} versus β at different δ_a

Collecting the results with β=0 in Table 5.2, a C_{Mz} versus β has been plotted in Figure 5.15. The adverse yaw genereted by a positive δ_a can be evaluated by obtaining the curve slope:

$$C_{Mx\delta_a} = -0.00016\, deg^{-1} \tag{5.4}$$

δa	Beta	CMz_WR	CMz_WFT
0	0	-2E-06	-0.0001
15	0	-0.00289	-0.00295
30	0	-0.00464	-0.00477

Table 5.2 – C_{Mz} values for different δ_a

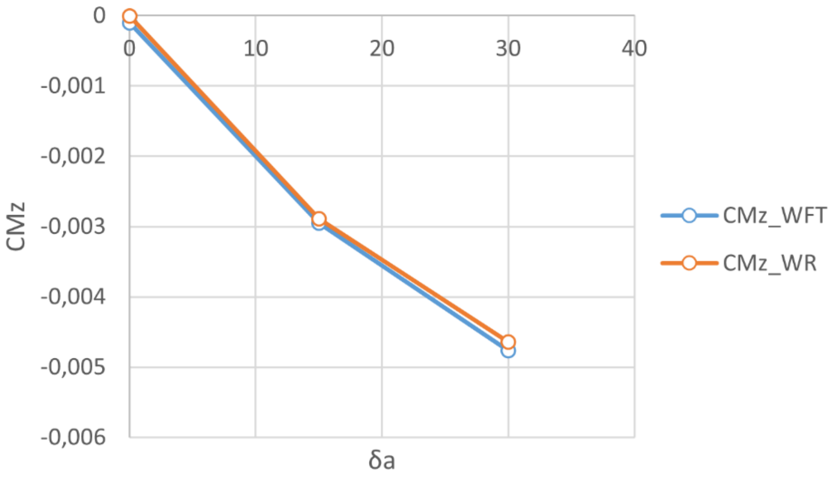

Figure 5.15 – C_{Mz} versus δ_a

5.4 Ruddervator effects on lateral directional aerodynamics

The ruddervator deflected asymmetrically functions as rudder, a positive δ_r means an upwards deflection of the left ruddervator and downwards for the right ruddervator, in this way the resulting force is a side force to the right that generates a positive yawing moment (Figure 5.16). The analyses have been done with the same flow conditions, the same β values, but at α=0°, and a δ_r of 0°, 5°, 10° and 15°. The deflection δ_r has been added using user parms (Figure 3.9).

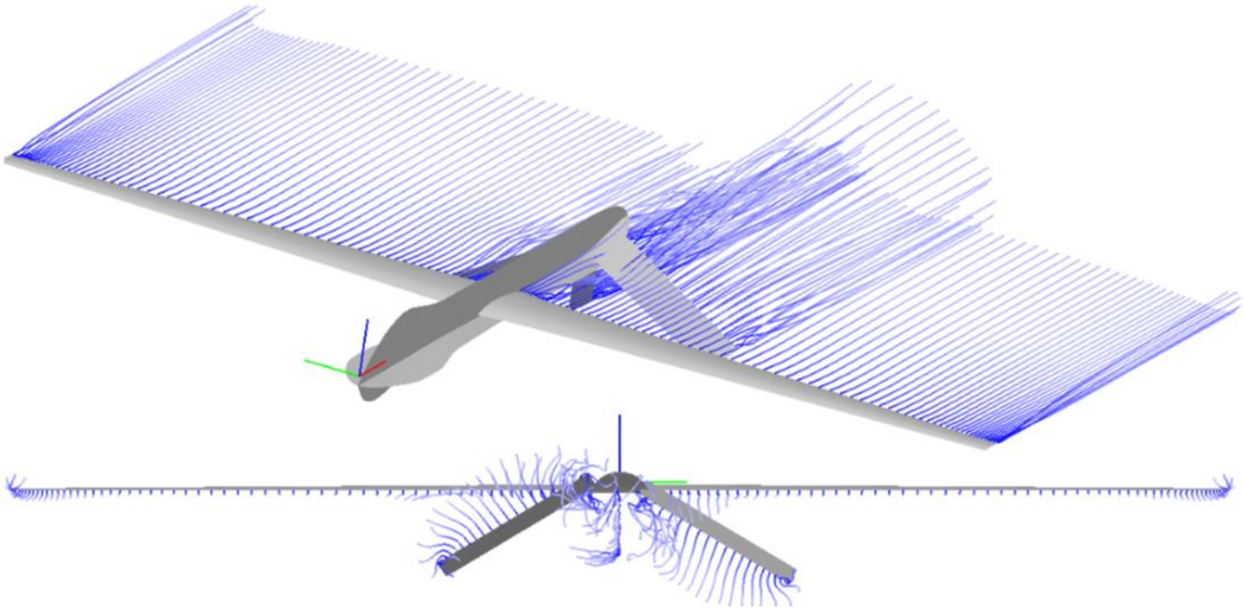

Figure 5.16 – Ruddervator deflected of δ_r=15° from VSPAERO viewer

5.4.1 *Wing and Tail Load*

The wing load (Figure 5.17) is not affected by δ_r, while on the tail the load increases on the right side and decreases on the left side.

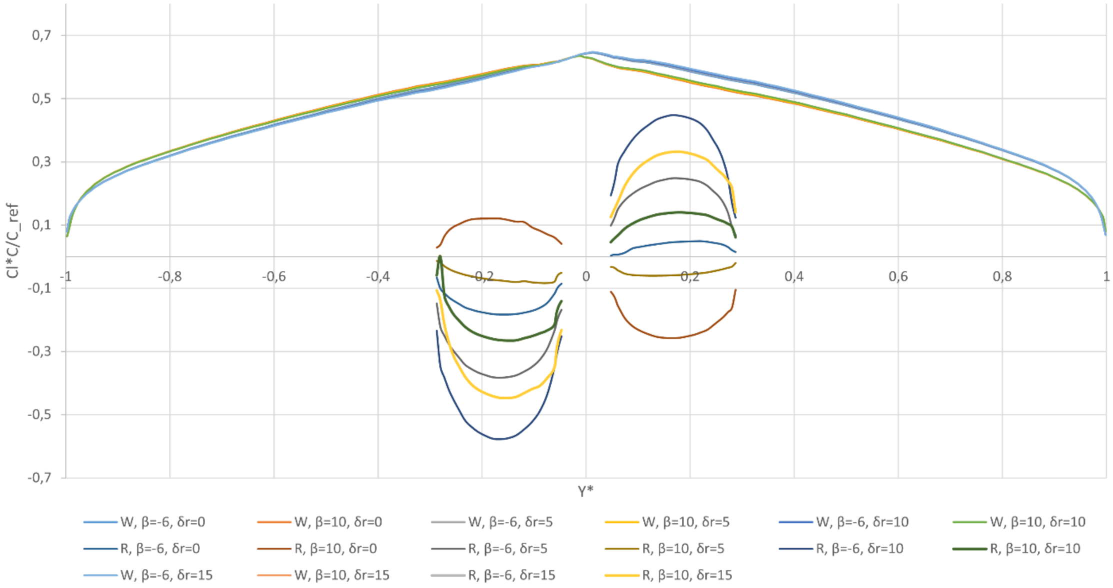

Figure 5.17 – Wing and tail load of WR set for different β and δ_r

5.4.2 *Pitching Moment*

C_{My} (Figure 5.18) maintain its trend with β and it decreases for positive δ_r. An interesting result is that an antisymmetric ruddervator deflection causes a significant rise in pitching moment, even at β=0°.

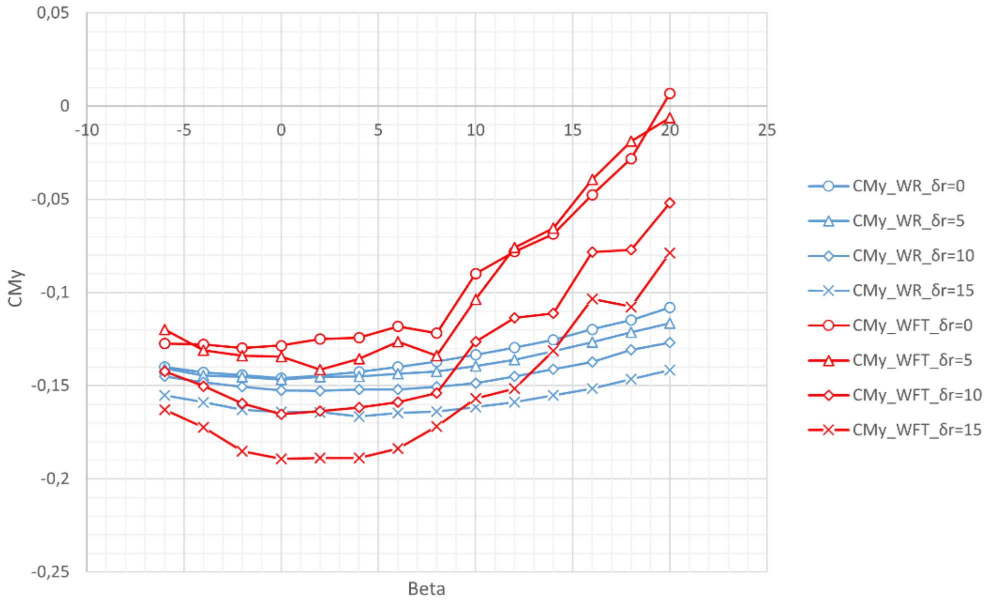

Figure 5.18 – C_{My} versus β at different δ_r

5.4.3 Rolling Moment

A positive δ_r means that the right half wing of the tail generates a positive lift, while the left one generates a negative lift, these two forces create a torque that generates a positive rolling moment as can be seen in Figure 5.19.

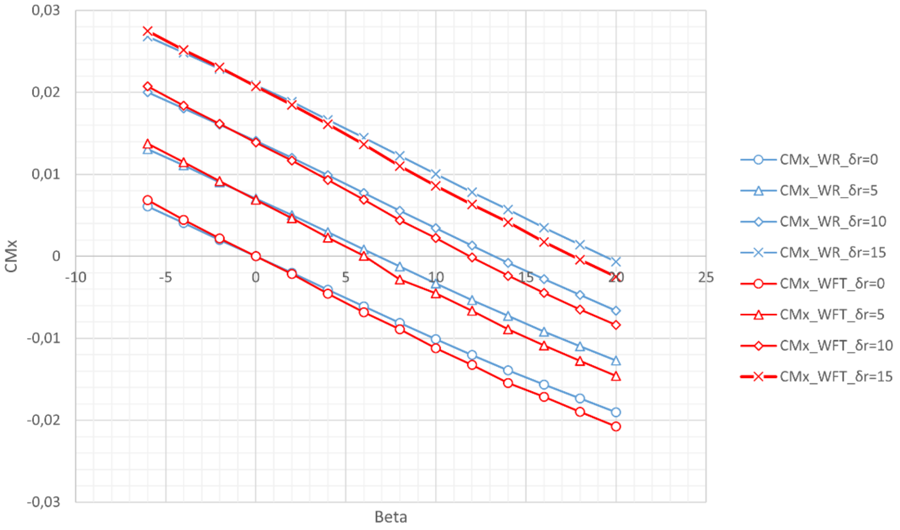

Figure 5.19 – C_{Mx} versus β at different δ_r

Plotting the C_{Mx} values at β=0° for differeny δ_r from Table 5.3, the chart in Figure 5.20 has been obtained. Evaluating the slope with Excel's slope function:

$$C_{Mx\delta_r} = 0.00138\ deg^{-1} \tag{5.5}$$

δr	Beta	CMx_WR	CMx_WFT
0	0	1.60E-06	1.57E-05
5	0	7.07E-03	6.92E-03
10	0	1.41E-02	1.39E-02
15	0	2.09E-02	2.07E-02

Table 5.3 – C_{Mx} values for different δ_r

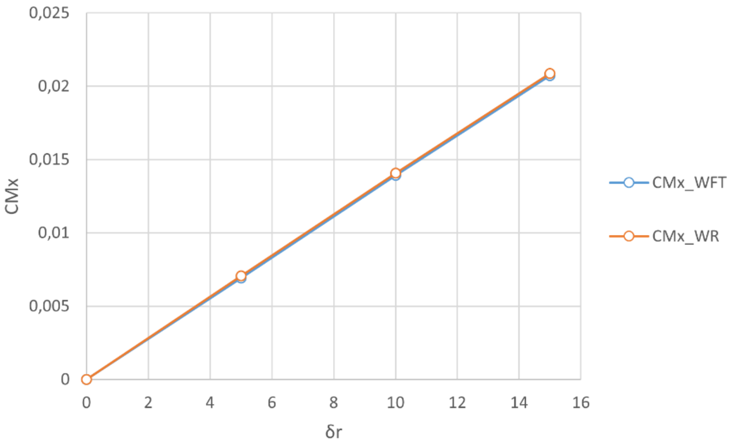

Figure 5.20 – C_{Mx} versus δ_r

5.4.4 Sideforce and Yawing Moment

As expected the sideforce C_{Fy} (Figure 5.21) increases for positive δ_r. Also C_{Mz} (Figure 5.22) increases for positive δ_r, so the aircraft to turn to the right have to deflect the ailerons with a positive δ_a and the ruddervator with a positive δ_r.

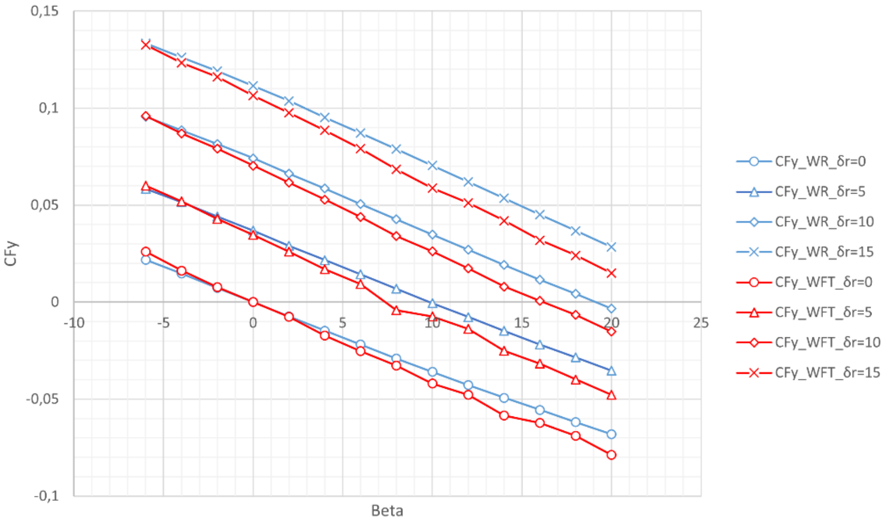

Figure 5.21 – C_{Fy} versus β at different δ_r

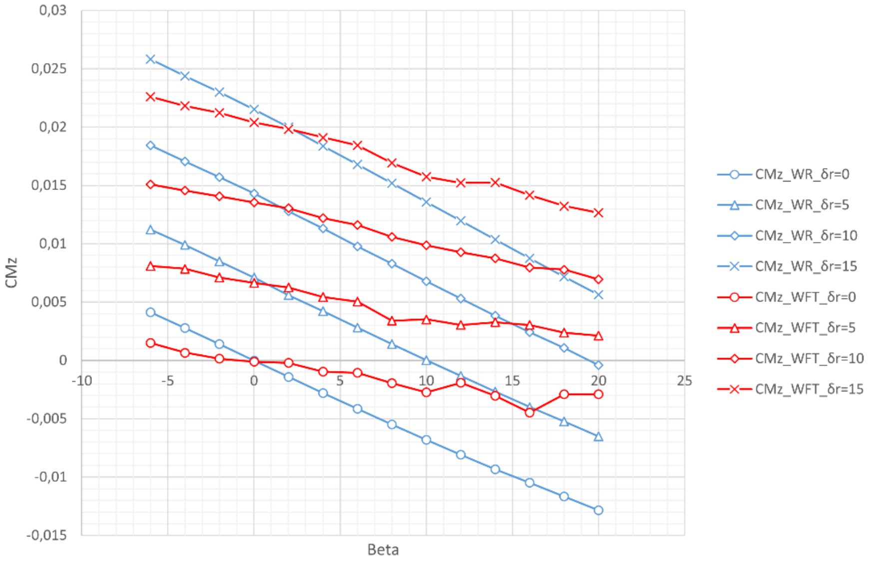

Figure 5.22 – C_{Mz} versus β at different δ_r

Set β=0, the data obtained are shown in Table 5.4 and in Figure 5.23.

δr	Beta	CMz_WR	CMz_WFT
0	0	-2.00E-06	-1.00E-04
5	0	7.12E-03	6.66E-03
10	0	1.43E-02	1.36E-02
15	0	2.15E-02	2.04E-02

Table 5.4 – C_{Mz} values for different δ_r

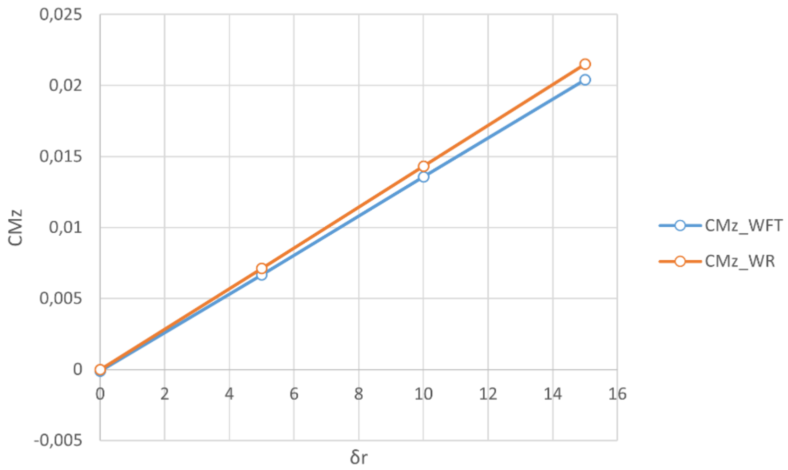

Figure 5.23 – C_{Mz} versus δ_r

Computing the slope it is possible to obatin the control derivative:

$$C_{Mz\delta_r} = 0.00137\ deg^{-1} \tag{5.6}$$

5.4.5 Results

It is possible to report in Table 5.5 all the obtained values.

C_{L0}	0.575	C_{My0}	-0.129	$C_{Mx\beta}$	-0.00107	$C_{Mz\beta}$	-1.91E-4
$C_{L\alpha}$	0.106	$C_{My\alpha}$	-0.0311	$C_{Mx\delta a}$	0.00421	$C_{Mz\delta a}$	-1.55E-4
$C_{L\delta f}$	0.0272	$C_{My\delta f}$	-0.00256	$C_{Mx\delta r}$	0.00138	$C_{Mz\delta r}$	0.00137
$C_{L\delta e}$	0.0154	$C_{My\delta e}$	-0.0364				
$C_{L\alpha\_Trim}$	0.0930						

Table 5.5 – The obtained results, the derivatives are measured in deg^{-1}

Conclusion

This thesis showed how it is possible to use OpenVSP software to perform a preliminary aerodynamic analysis of an aircraft using the VSPAERO tool. It was possible to estimate static stability and control derivatives to evaluate the longitudinal and latero-directional stability of the aircraft. The VSPAERO tool provided many reliable aerodynamic results quickly and easily. The aerodynamic model that can be deduced from the results of the analysis is complicated by the presence of a V-shaped tailplane (straight or inverted), because the latero-directional controls are strongly coupled and they also affect the longitudinal equilibrium, even assuming that such model is constructed linearly. A possible development of this thesis would be to compare these results with those obtained from advanced CFD software or wind tunnel tests.

Bibliography

[1] Advanced UAV aerodynamics, Flight stability and control, Pascual Marqués, Andrea Da Ronch Jon Wiley & Sons, Apr 27,2017.

[2] OpenVSP website: http://openvsp.org.

[3] Software Testing: VSPAERO, Floris Mariën, Prof. Dr.-Ing. Dieter Scholtz, 16/07/2021.

[4] VSPAERO theory, avid Kinney, 2020 OpenVSP Workshop, 16/09/2020.

[5] Department of the Air Force, Engineering Technical Letter (ETL) 09-1: Airfield Planning and Design Criteria for Unmanned Aircraft Systems (UAS), 2.

[6] Airfoil Tools website: http://airfoiltools.com.